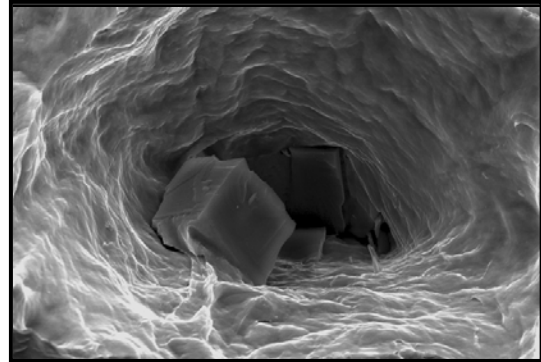


Stainless steel damage study using Digital Imaging Correlation and Orientation Imaging Microscopy

S. Boonstra (1453505)
J. J. van den Berg (1380931)

February 11th – May 13th 2008

Abstract



Damage accumulation during plastic straining of new type of stainless steel JYH21CT is studied experimentally. For a comparison AISI 410 stainless steel is examined too. Both steels are alpha-iron with chromium solute in a state after soft annealing. A special shape of the tensile sample was used to generate a gradient of plastic strain after failure in tensile test. Digital Image Correlation technique was used to characterize the local plastic strain and Orientation Imaging Microscopy (OIM) to quantify accumulation of plastic deformation inside ferritic grains.

Standard experimental methods as SEM observation of fractographic surfaces, quantitative optical and SEM metallography observation of voids, X-ray diffraction, EDS measurement and hardness measurements were also used.

Fractographic observations reveal that TiN inclusions in JYH21CT steel act as void nucleation sites. The Grain Orientation Spread (GOS) has been found as a good parameter to correlate damage to plastic strain. It is the average misorientation angle within a grain given by OIM analysis. The GOS distribution of a large population of grains has a log-normal distribution. Both Aramis and OIM observations suggest that there are two regions with plastic deformation and damage accumulation. The first region is below 20% of strain and is characterized by a slow strain rate and fast accumulation of the grain orientation spread. In the second region, above 20% of strain, the strain rate is higher and the grain orientation spread grows slower in bulk grains and fully stops to grow in surface grains.

1. Introduction

A recently introduced stainless steel called JYH21CT is a potential candidate to be applied in a deep drawn steel boiler for steam ironing by Philips Drachten. In order to successfully model the behavior of this steel during processing a careful study of the damage mechanisms is vital. It is suggested that voids and small inclusions in the material may contribute to damage by strain.

In this report the results of a strain induced damage study on JYH21CT are presented. The goal is to find one or more parameters that can describe damage. The more commonly applied stainless steel AISI410 will be used as a reference material.

The main experimental techniques that have been used are Digital Image Correlation (DIC) of step-by-step recorded images of the surface of the tensile sample in combination with examination of microstructure at different strains using Orientation Imaging Microscopy (OIM). Additionally observations of the deformed material have been made using Optical Microscopy (OM) and Scanning Electron Microscope (SEM). X-ray diffraction and Energy Dispersive X-ray Spectroscopy (EDS) have been used to characterize the materials. Also some bent samples have been investigated using OIM, OM and SEM and hardness measurements have been performed.

2. Table of contents

1. Introduction	-2-
2. Table of contents	-3-
3. Experimental procedures	-4-
3.1 Tensile test sample shape	-4-
3.2 Bending experiment and samples	-4-
3.3 Tensile test and strain measured by Digital Image Correlation	-4-
3.4 Sample cuts and preparation	-6-
3.5 SEM and EDS	-7-
3.6 OIM experimental technique	-7-
3.7 X-ray diffraction	-10-
3.8 Hardness measurement	-10-
4. Results	-11-
4.1 Material properties	-11-
4.2 Tensile experiment with MTS machine	-17-
4.3 Aramis experiments	-17-
4.4 Fractography	-24-
4.5 Voids in JYH21CT	-27-
4.6 OM observations	-29-
4.7 OIM observations	-33-
5. Discussion	-38-
6. Conclusions and recommendations	-43-
7. Acknowledgements	-44-
8. References	-45-
Appendix	-46-

3. Experimental Procedures

3.1 Tensile test sample shape

The samples used for the tensile tests were shaped as shown in Figure 3.1 with a narrow necking about two centimeters next to the middle, getting broader towards the other end. Whilst under tension such a sample will undergo different strains across the length of the sample. This makes it possible

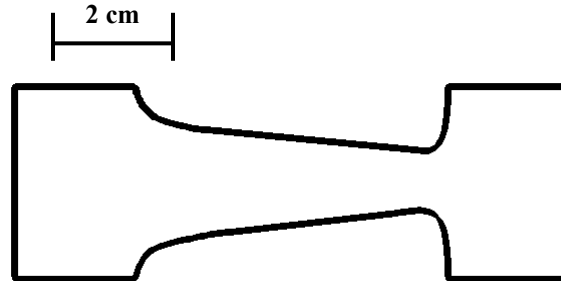


Fig 3.1. Tensile test sample

to study the microstructure and damage for plastic strains after the tensile test varying from low strain till the fracture strain, using only one sample. AISI410 samples with a thickness of 0.5 mm have been used for testing, the JYH21CT samples were 1.5 mm thick. The length of the samples was 95 mm. Three samples have been tested for both steels.

3.2 Bending experiment and samples

To study the deformations after bending of the steel, samples have been bent with a bending curve of radius 1.5 mm. These samples have been studied using Optical Microscopy (OM) and some hardness tests have been performed.

3.3 Tensile test and strain measured by Digital Image Correlation

An MTS 810 Materials Test System tensile machine has been used to perform tensile tests on the samples of both steels. During the tensile experiment one machine clamp is fixed, while the other is moving upwards with a constant velocity. Meanwhile the load on the sample is measured. The tensile experiment is performed until fracture. In this experiment the clamp has been moved up with a constant velocity of 0.021 mm s^{-1} . This means an engineering strain rate of $2.2 \cdot 10^{-4} \text{ s}^{-1}$.

To record the deformation of the different samples during tensile testing, the Aramis – Digital Image Correlation (DIC) system is used. This system takes step-by-step pictures of the surface under deformation. These images are then analyzed using the

Aramis software, after which the local strain field can be calculated from 3D displacements on the surface of the sample.

Two cameras are used to make a series of images of the sample under a different angle. The samples are painted with black dots randomly distributed on a white substrate. The Aramis software is able to identify the dots of the random pattern on the images taken.

The first step is to take an image obtained with say the left camera. On this image software creates small squares of a few pixels called facets. The image of the sample is filled with these facets, covering the whole surface.

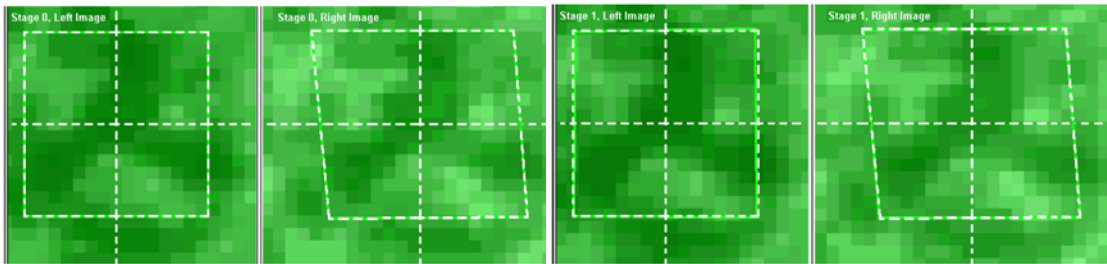


Fig 3.2a. The Aramis software recognizes the same facet on the surface of the left and the right camera image. Facets with a size of 15 pixels have been used in this example. [1]

Fig 3.2b. Left and right image facets have a small difference with Fig.2.2a. From this the Aramis software calculates the strains on the surface of the sample. [1]

The Digital Image Correlation algorithm of the software is used to detect the facets covering the same area on the sample surface on the left and right image (Figure 3.2a). Next this facet filled image is taken as a reference to fill images in later stages with an equal amount of facets covering the same, now deformed area. DIC is used to correlate the images in later stages (Figure 3.2b with the first (undeformed) one) and also to correlate left and right image in every stage. Thus every image in every stage is covered with facets. For the software to work properly the strains must change quasi-static, i.e. no sudden changes or jumps of the facets.

Now the position of each facet is calculated. From the displacement of each facet center between individual steps, the local strains on the surface of the sample can be calculated. In this report calculations were performed using a facet size of 11 pixels with a spacing of 7 pixels (an overlap of 4 pixels). The images were taken every second or every two seconds.

In this report the term technical strain will be frequently used. It is defined as Δ/L , the difference in length divided by the initial length. Furthermore a clear distinction will be made between engineering (macroscopic) strain and true (local) strain. Strain in the tensile direction is called major strain. Strain in the direction of the width of the sample is called minor strain.

It is possible to use the output signal of the MTS machine via a trigger box to link the load on the sample to these strains during the experiment and consequently draw a stress-strain curve. [1]

3.4 Sample cuts and preparation

Investigations on the surface of the AISI 410 and JYH21CT steel sheets have been done on samples which have been electrochemically polished. With this polishing method, the sample is brought into contact with an electrolyte. The electrolyte contains an electrode which acts as the cathode, the

sample is the anode. Applying a voltage between the anode and the cathode will cause a reaction within the cell which will remove a thin layer of the surface of the sample. The electrolyte that has been used is called A3 in Struers nomenclature, which is a 6% perchloric acid solution in a mixture of methanol and butoxyethanol. A voltage of 20 V was applied for 60 seconds.

The cutting of the fractured tensile samples for microscope observations is shown schematically in Figure 3.3. The cutting has been done on a diamond saw with a thin blade and at a low speed to reduce the damage induced by the cutting as much as possible.

To examine the cross-section through the thickness of the sample, the longer side of part A has been used. On this side the search for voids and a lot of OIM scans (which will be explained later on) have been performed. The OIM experiments require a surface without any damage generated by the sample preparation. Mechanical polishing has been used, consisting of a quarter of an hour polishing with SiC-paper of grain size 1200, followed by polishing with 9 μ , 6 μ and 3 μ diamond paste, also for fifteen minutes. The finishing touch is given by a polishing treatment with a SiO₂ suspension for about an hour. Ten minutes of polishing solely by water is needed to remove particles of the SiO₂ suspension from the area of interest.

Part B of the sample has been used to perform OIM scans on the outer or free surface

of the sample. Because necking plays a serious role near the fracture, the surface of this part isn't flat at all. While decent mechanical polishing of a rounded surface is almost impossible, electrochemical polishing with the previously mentioned electrolyte A3 has been used here.

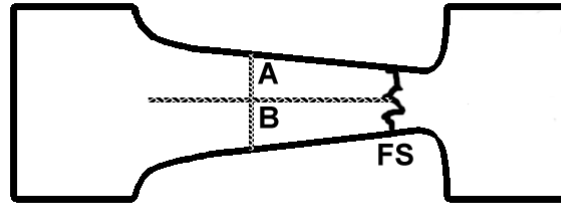


Fig 3.3 Cutting of fractured tensile samples where A and B mark the different parts and FS is the fracture surface



Fig 3.4 Cutting of undeformed samples, where A and B mark the different parts and the red arrows indicate the side that has been investigated

Some observations on an undeformed sample have been done. This sample's cutting is shown schematically in Figure 3.4. The sides indicated with red arrows have been investigated. On both sides the previously explained mechanical polishing method has been used.

3.5 SEM and EDS

To have a look at features of a sample which can't be distinguished by an optical microscope, the Scanning Electron Microscope is a very powerful tool. An image is acquired by detecting the secondary or back-scattered electrons that are generated from the surface by the primary electrons from a highly focused electron beam with energy between 3 and 30 kV. Together with continuous scanning of the sample surface, the user of the SEM is provided with high resolution images of the surface examined.

When the primary electrons have enough energy to penetrate the inner electron shells of the atoms in the specimen, these atoms will be ionized by the process described before. Shortly after ionization, they will go back to the ground state by filling the hole left by the excited electron with an electron from the outer shell. This is accompanied by the emission of an X-Ray, which has an energy that depends on the atomic number of the particular atom. Therefore, by collecting the X-Ray spectra, a chemical analysis of the surface is possible in an SEM. This is called Energy Dispersive X-ray Spectroscopy (EDS).

In this research the secondary electron detection in the SEM has been used for fractography and void search. The microscope used is a Philips XL-30 FEG. EDS has been used to determine which elements are contained by the inclusions in the material. The system used is a Philips XL-30 FEG with an Edax EDS detector.

3.6 OIM experimental technique

OIM is an abbreviation for Orientation Imaging Microscopy and is a technique that uses the SEM and Electron Backscattered Diffraction (EBSD) to determine the crystal orientations at the sample surface. To do this, the SEM electron beam is aimed at the surface of interest. The beam hits a reasonable small area and penetrates it for a few tens of nanometers. A fraction of these electrons is inelastically scattered by the atoms in the material, creating a source of electrons from the sample surface in all directions. The scattered electrons can be diffracted from the lattice planes which characterize the crystal orientation. For this to happen, they have to satisfy the Bragg Condition:

$$n\lambda = 2d \sin \theta \quad (\text{Eq 1})$$

where n is an integer, λ is the wavelength of the electrons, d is the spacing between the lattice planes and θ is the Bragg angle. When this condition is satisfied, constructive interference takes place, creating two so-called Kossel cones, one from the top of the diffracting plane

and one from the bottom of the plane. (They are cones because the electrons are scattered in all directions) (Figure 3.5)

To detect the diffraction bands caused by these two cones, a fluorescent screen is placed near the examined surface. The crystallography of the examined point is revealed by the projection on the screen of the cones originating from all the different planes belonging to the crystal structure. The pattern that is formed in this way is called a Kikuchi-pattern. (Figure 3.6)

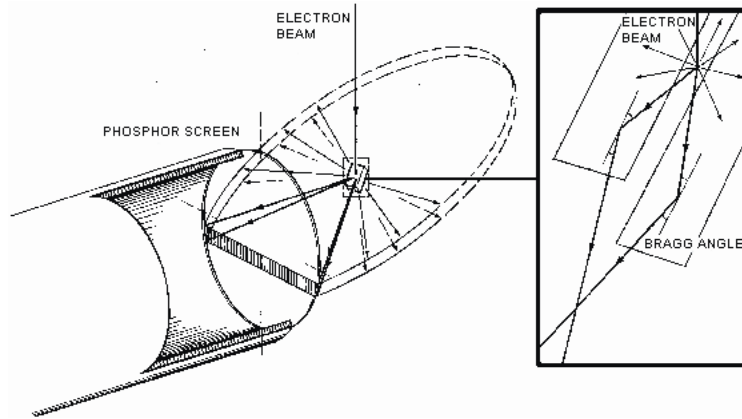
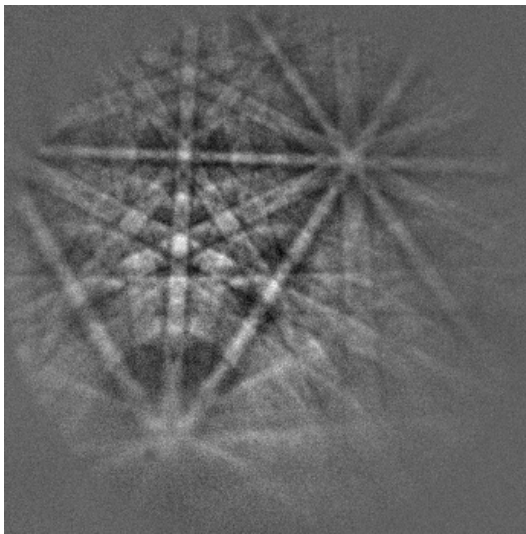
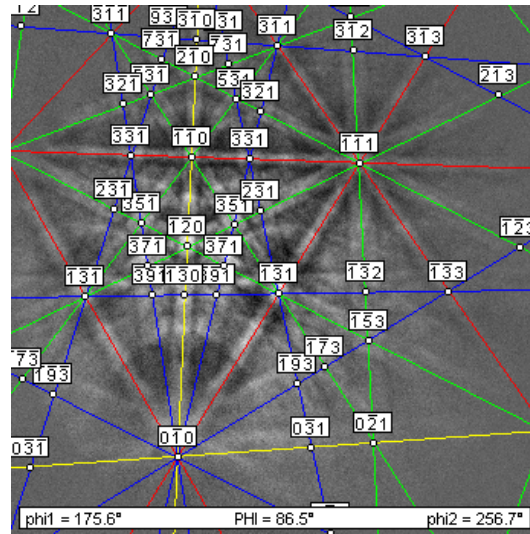


Fig 3.5 Formation of the EBSD pattern. Electrons diffract and form cones when the Bragg condition is satisfied [2]



(a)



(b)

Fig 3.6(a) Image of a Kikuchi pattern of the alpha-ferrite chromium phase retrieved from the CCD camera behind the phosphor screen. (b) The same image showing the bands and the indexes of the planes that belong to them, recognized and calculated by the software.

Pattern indexing

The software is able to recognize the different bands and to calculate the angles between them. These angles are typical for different crystals. Once the phases of the material are known and the quality of the Kikuchi pattern is sufficient, the software can index the patterns (Figure 3.6b) and select the best fitting phase from a list of possibilities given by the user. The crystal orientation is determined in the coordinate system depicted in Figure 3.7.

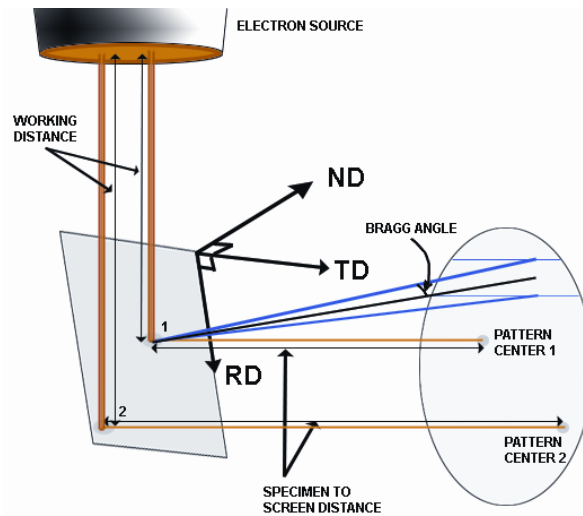


Fig 3.7 Schematic representation showing the definitions of working distance, specimen to screen distance and the sample coordinate system

To retrieve the best interpretation of the images, the system needs to be calibrated. The pattern changes when the distance between the electron source and the sample is changed (See Figure 3.7). This so-called working distance determines the position of the pattern center on the screen and is one of the main variables for calibration. Another main aspect of the calibration is to determine the specimen to screen distance. This distance is like a magnification factor for the pattern, so it determines the width of the bands and the distance between them, as can be seen from Figure 3.7. Whilst the angles between the bands, their width and their spacing are known, the software can simulate the pattern indexing for a certain orientation. It then picks the best match between all possible simulated indexing patterns and the measured pattern. The discrepancy between the chosen simulated pattern and the real pattern is a measure for the accuracy of the indexing.

To couple the orientations found by the indexing software to the sample orientation, a coordinate system of the sample is defined. This coordinate system is also shown in Figure 3.7. Here ND stands for the normal direction perpendicular to the sample surface, RD is the rolling direction along the sample surface and TD is the transverse direction along the sample surface and perpendicular to the rolling direction.

EBSD performs best when the sample is tilted 70° from the horizontal, because this gives the best yield of backscattered electrons. The beam can be controlled by the software, thus making it possible to scan and index an area of the sample automatically. By moving the beam over the sample, the pattern center on the screen also moves. The software can correct for this movement automatically using the

calibration parameters and the position of the beam given by the SEM.

System setup

The scans in this research have been performed on a Philips XL-30 FEG system. The electron beam had an accelerating voltage of 20 kV and a spot size of 5. The typical size of the scanned area is about 10 – 300 μm , while the typical indexing time is 13 points per second.

The only phase present in the material is alpha-iron chromium, which is body-centered cubic. The group symmetry of this phase is cubic(0h)(m3m). The reflectors used are listed in Table 3.1. The estimated total microscope time used for the OIM scans in this research is 300 hours.

hkl	d-spacing
110	2.036
200	1.440
211	1.176
310	0.911

Table 3.1 Reflectors of the α -FeCr phase used in OIM scanning.

Experiments

Experiments have been done on the surface of electrochemically etched samples of both steels to determine average grain sizes and the possible occurrence of texture. On the JYH21CT tensile sample, a lot of scans of equal area have been performed at different distances from the fracture surface. The strain at these points is given by the Aramis experiment, which gives the possibility to correlate the scan results to a certain amount of strain. [2,3]

3.7 X-ray diffraction

Philips X-ray Powder Diffractometer with a Cu X-ray source was used to detect phases in both tested steels.

3.8 Hardness measurement

A Vickers hardness measurement with a 4 N load has been performed on the JYH21CT steel.

4. Results

4.1 Material properties

Phase analysis by X-ray diffraction

In Figure 4.1a and b the diffraction patterns of AISI410 and JYH21CT respectively can be seen. The figures show at what angle peaks can be found, while the intensity is just a value in arbitrary units. The measured patterns correspond quite clearly to the iron chromium phase profile from the database, shown in red. The materials both consist of BCC iron crystals with chromium solution. The lattice parameter $a = 2.876 \text{ \AA}$, the JCPD number of this phase is 34-0396. The Figure of Merit, a quality factor which indicates the agreement between experiment and theory with a number between 0 and 1, equals 0.71 for AISI410 and 0.73 for JYH21CH. In the figure the plane identified with each peak is given. Two peaks at the same angle, but with a different intensity indicate a difference in texture. This peak identification is performed using the computer program Match!

These X-ray diffraction measurements confirm that both steels are investigated in state after soft annealing, i.e. austenitization and slowly cooling down.

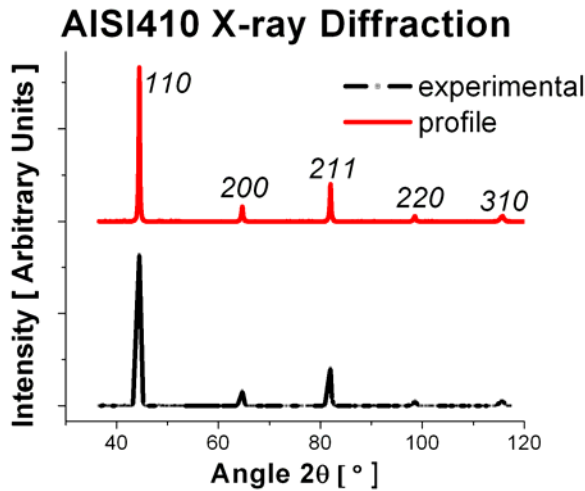


Fig 4.1a X-ray diffraction pattern of AISI410 steel.

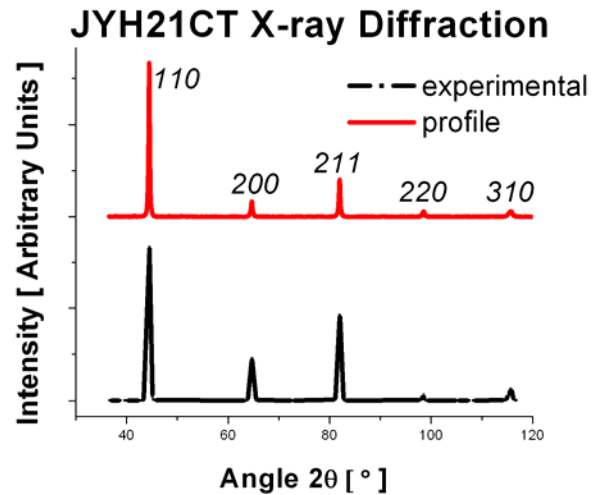


Fig 4.1b X-ray diffraction pattern of JYH21CT steel.

Inclusions in JYH21CT steel by OM

(Figure 4.2 OM-inclusions) shows an optical microscope image taken from a JYH21CT steel sample. Inclusions with a size of about 3 μm can be observed. The inclusions are clearly faceted.

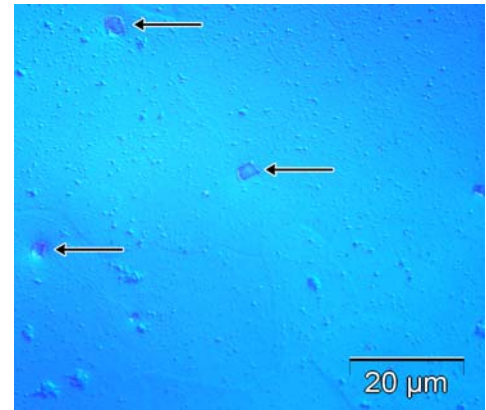


Fig 4.2 Inclusions in the JYH21CT steel

Inclusions in JYH21CT steel by EDS

EDS spectra of the inclusions found in the OM and SEM observations on the JYH21CT steel have been used to determine of which elements these inclusions consist. The results of the spectrum analysis of 3 different inclusions are shown in Table 4.1. From these results we conclude that the inclusions contain the elements titanium and nitrogen in the ratios 2:1, 3:1 and 3:2.

The portions of iron and chromium are from the material surrounding the inclusion.

These portions appear because the spot of the electron beam is too large to aim it only at the inclusion. The small portion of oxygen that appears at point 3 is assumed to be caused by a bit of oxidation at that point.

It is concluded that the inclusions are non-stoichiometric TiN particles.

Element	Point 1 At %	Point 2 At %	Point 3 At%
N	21.51	23.61	19.74
O	0	0	3.7
Ti	56.28	67.57	30.97
Cr	7.54	2.76	11.85
Fe	14.68	6.06	33.73
Total	100	100	100

Table 4.1 EDS results for 3 different inclusions in the JYH21CT steel

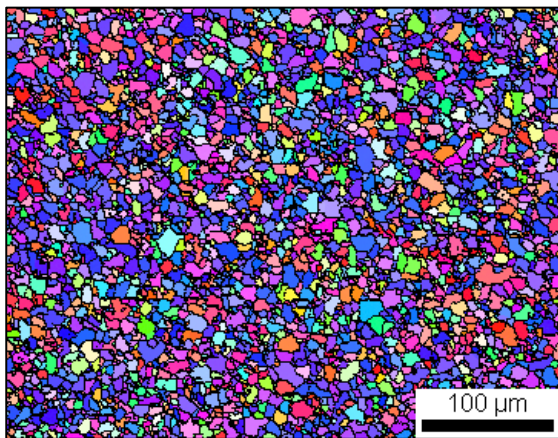
Grain size by OIM

The surface of undeformed samples of AISI 410 and JYH21CT steel are scanned using OIM to learn more about the general features of the material. Figure 4.3 shows parts of these 2 scans. The complete scans are performed on an area of 500 x 1000 μm . For all scans in this research the tolerance angle was 5 degrees, which means that two neighboring points are considered to be in different grains when their orientation differs more than 5 degrees. Between all the points satisfying this condition a grain boundary can be drawn. The grain diameter statistics are performed on the whole scan.

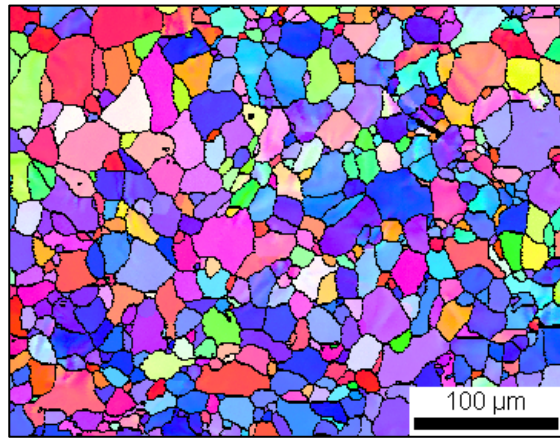
This figure shows clearly that the grain size of AISI 410 is much smaller than that of JYH21CT. The average diameter of the AISI 410 grains is 9 μm , while the average grain diameter of JYH21CT is 22 μm . To calculate the grain diameter, the total area of the grain is calculated first. Then the grain is assumed to be a circle, and the diameter is calculated by taking 2 times the square root of the area divided by π . The

distributions of the grain size for both scans are shown in Figure 4.3c and d. These distributions can be fitted with a log-normal distribution from which the average grain size and its standard deviation can be determined.

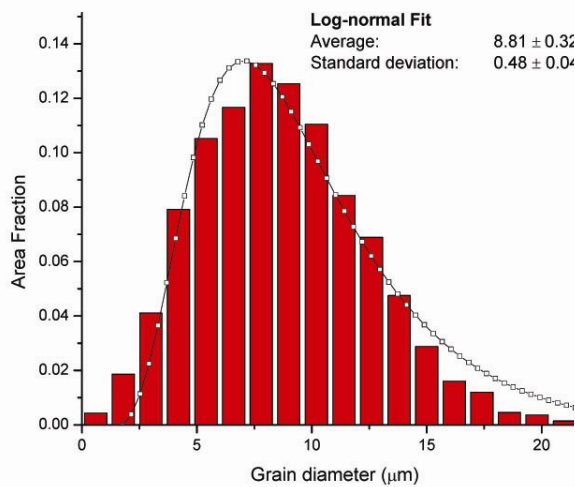
There appear some black spots inside individual grains in Figure 4.3b, the Inverse Pole Figure Map of the JYH21CT steel. These are non-indexable points which often indicate the presence of an inclusion. Both figures show a lot of blue colors, which indicates a preference of the [111] orientation parallel to the surface normal direction (see legend in Figure 4.4). This is investigated further in the paragraph ‘Texture by OIM’.



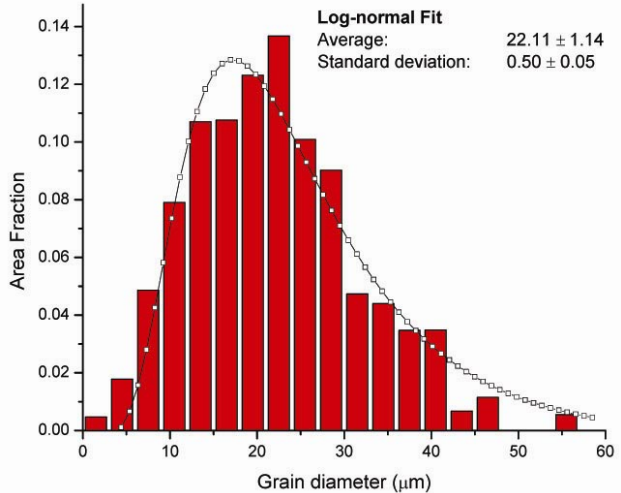
(a) Average grain diameter: 9 μm .



(b) Average grain diameter: 22 μm .



(c) Grain size distribution of AISI 410



(d) Grain size distribution of JYH21CT

Fig 4.3 Inverse Pole Figure Maps of OIM scans of the surface of (a) AISI 410 and (b) JYH21CT steel sheet samples. (legend in Figure 4.4) Grain size distributions of the full area of these scans: (c) AISI 410 and (d) JYH21CT steel.

Grain shape of JYH21CT

This paragraph concentrates on the grain size and shape of JYH21CT steel from three different sides. Figure 4.4 shows parts of 3 scans on the undeformed JYH21CT steel sample. The surface on which each scan is taken is indicated schematically on the sample in the figure. Their nomenclature corresponds to those in the description of the sample cuts and preparation. Statistics of grain size and shape are performed on the full area which is not completely shown here. The full scan in the bulk of the sample was performed from the surface till the center for sides a) and b). Later on in this report, the grain shape of the JYH21CT steel will be investigated as a function of strain on the surface similar to a).

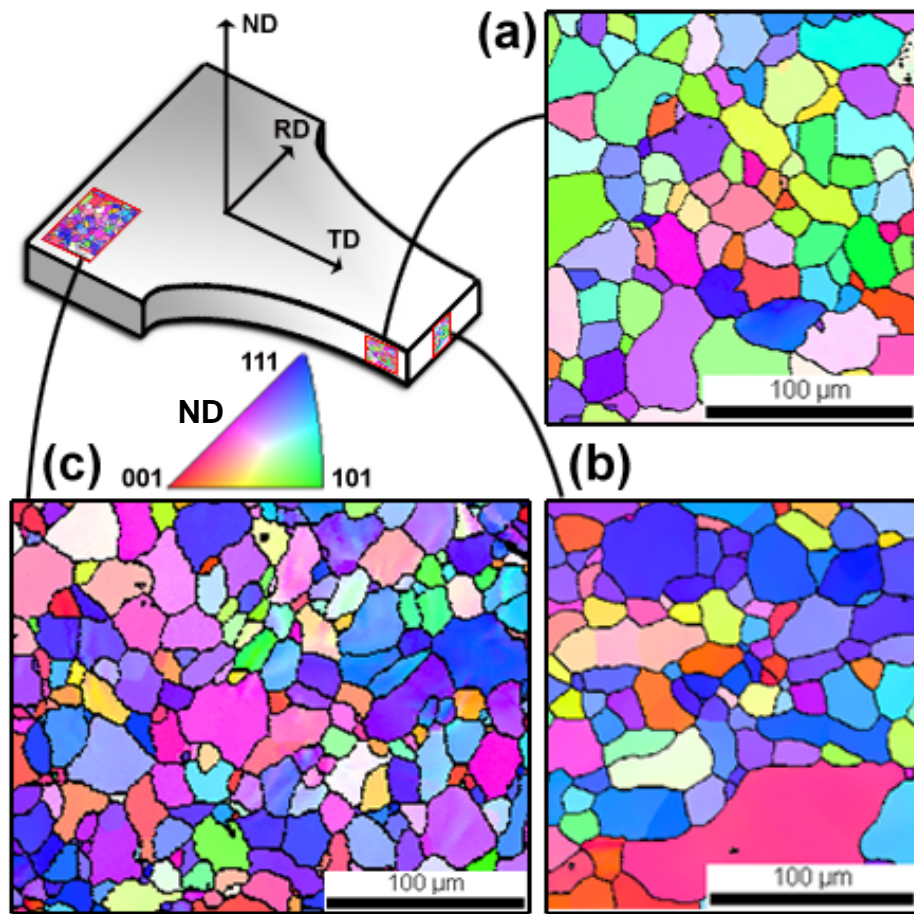


Fig 4.4 OIM scans performed on different sides on undeformed JYH21CT steel. Characters assigned to each scan correspond to the names of the samples described in 'Sample cuts and preparation'.

Table 4.2 gives the average grain diameter and average grain shape aspect ratio (see Appendix) calculated by the software for the full area of the scans shown partly in Figure 4.4.

The grain shapes are similar when looking from different sides at the sample. There are no substantial differences in grain size and grain shape aspect ratio observed on different cuts of the JYH21CT sample.

Side	Grain Diameter (μm)	Grain Shape Aspect Ratio
a)	28	0.53
b)	28	0.55
c)	22	0.53

Table 4.2 Results of calculations on the full scans of Figure 4.4. Both parameters are averages over all grains.

Texture by OIM

The crystallographic orientations of a material can be randomly distributed, but they can also show one or more preferred orientations. When this is the case, the sample shows a texture which can be weak, moderate or strong. Because a lot of grains of the same color have been found in the scans shown in Figure 4.4, the two materials should show some degree of texture. To prove this, the texture plots of the $[111]$ direction are shown in Figure 4.5 for free surface scans on both steels.

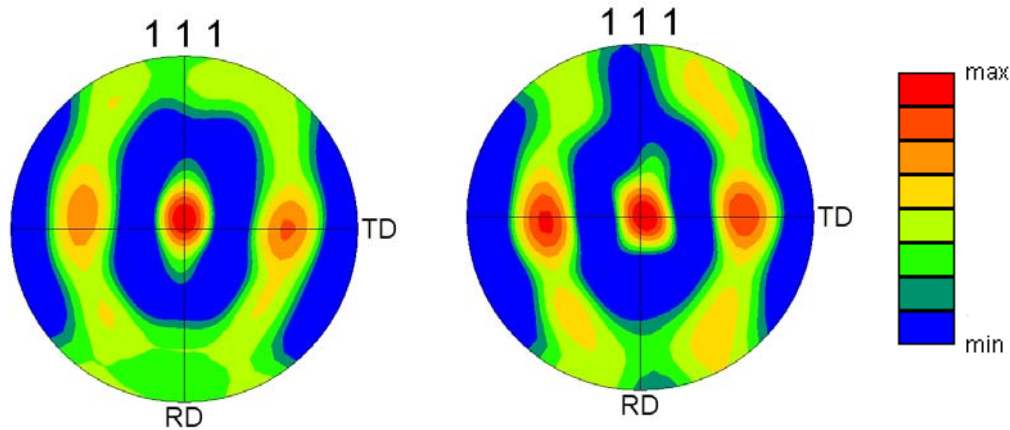


Fig 4.5a 111 Texture plot for the surface of AISI 410 steel

Fig 4.5b 111 Texture plot for the surface of JYH21CT steel

The red dot in the center of the texture plots indicates that the crystal is preferably oriented with the $[111]$ direction parallel to the normal direction of the sample surface. When looking straight at the sample surface, the crystal orientation should be like it is indicated schematically in Figure 4.6a. To proof that this corresponds to the texture plots, Figure 4.6b gives the position of the dots in the pole figure for this orientation. Comparing this figure with the texture plots of Figure 4.5, one can see that the crystal is allowed to rotate as indicated by the arrows. The

complete rotation is not allowed though in JYH21CT, which can be seen from the blue part at the top of the texture plot in Figure 4.5b. Furthermore, there is a preference of the orientation shown in Figure 4.6a and b, and its 180° rotated counterpart. This preference is indicated by the red dots along the TD of the texture plots.

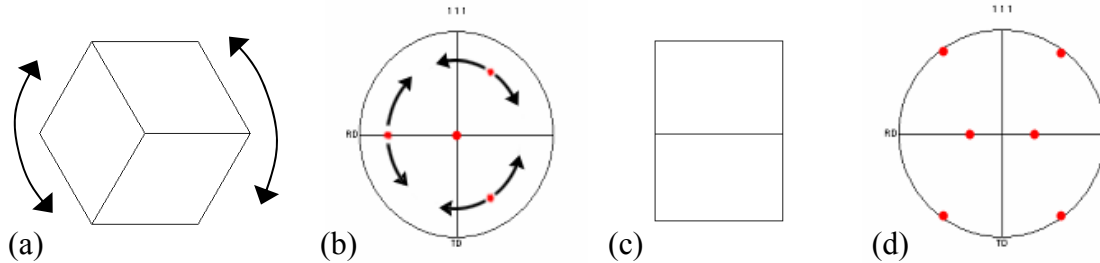


Fig 4.6 Crystal orientations (a) and (c) and their respective pole figures (b) and (d) belonging to the texture plots in Fig 4.5.

The just mentioned preferred orientations would have caused spots in the center of each quadrant of the texture plots with the same density as the three on the TD axis. Since this is not the case, there should be another preferred orientation causing the two outer dense spots along the TD axis. The only candidate found for this to happen is shown in Fig 4.6c. The spots in the pole figure belonging to this orientation are shown in Fig 4.6d. The presence of this orientation also explains the nonzero densities at the top and bottom edge of the texture plots.

The texture analysis confirms that both steels have a very similar texture composed from:

- $\langle 111 \rangle \parallel \text{ND}$
- $\langle 001 \rangle \parallel \text{TD}$ & (001) inclined 45° to ND.

4.2 Tensile test experiment with MTS machine

Figures 5a and 5b show the so-called engineering stress-strain curves measured in samples of AISI410 and JYH21CT steels. The engineering or macroscopic strain is based on the deformation of the whole sample, in comparison with the initial length. The engineering stress corresponds to the measured load acted on the smallest, critical sample cross-section. The tests took respectively 300 seconds and 367 seconds.

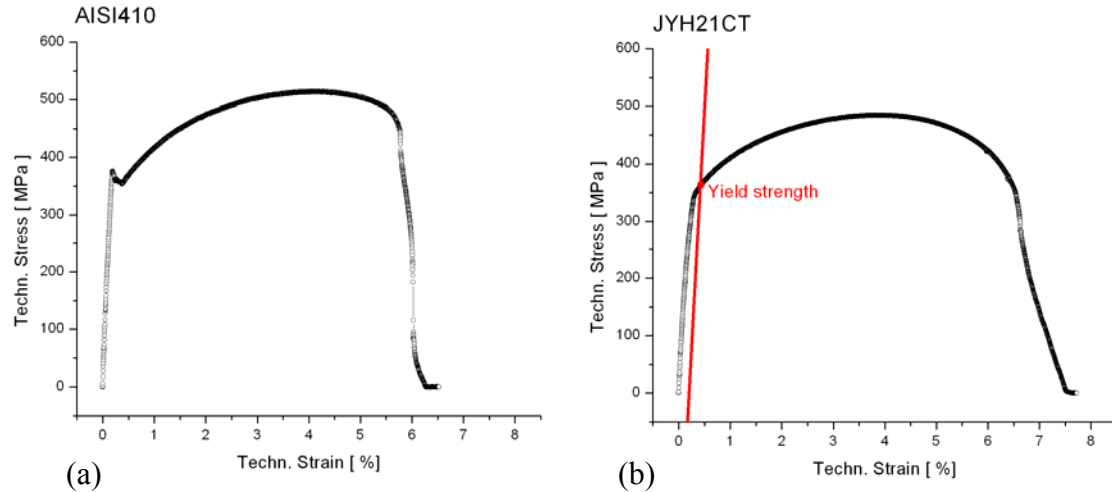


Fig. 5a and b. Engineering stress-strain curves of AISI410 steel (a) and JYH21CT steel (b). The latter shows how yield strength is determined.

The AISI410 steel has a distinctive elastic-plastic transition at about 0.2 % (macroscopic) strain, with an upper yield point of 375 MPa. The JYH21CT steel has a yield strength of 366 MPa at 0.5% (macroscopic) strain, determined by the intersection with a straight line parallel to the elastic segment of the curve with a translation of 0.2 %. The maximum strength is determined to be 510 MPa for AISI410 and 480 MPa for JYH21CT. Final fracture was obtained at 6 % strain for AISI410 and 6.5 % for JYH21CT.

4.3 Aramis experiments

Strain overlay on JYH21CT

Figure 4.8 shows an image of a JYH21CT sample with an overlay of the major strain field (local strain ϵ_y ,

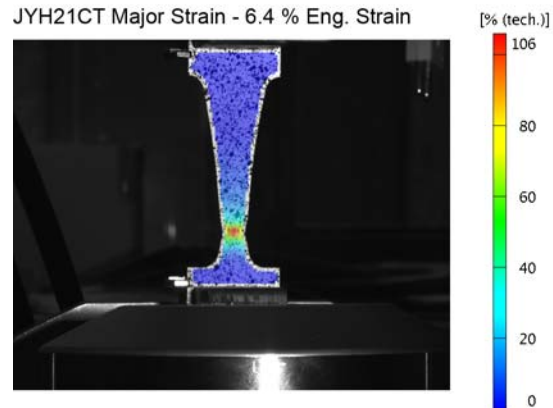


Fig 4.8. Overlay of the major strain on the left camera image of a JYH21CT steel sample right before fracture.

the y-direction being in the tensile test direction) with a macroscopic strain of 6.4%, i.e. right before fracture. A big increase of the local strain up to about 100 % on the surface near the fracture area can be seen. Information of the whole experiment (images taken every 2 seconds) is available also for the AISI410 steel, which has similar behavior.

Figure 4.9a-d show the fields of all strain components at the surface of JYH21CT at 6.4% engineering (macroscopic) strain.

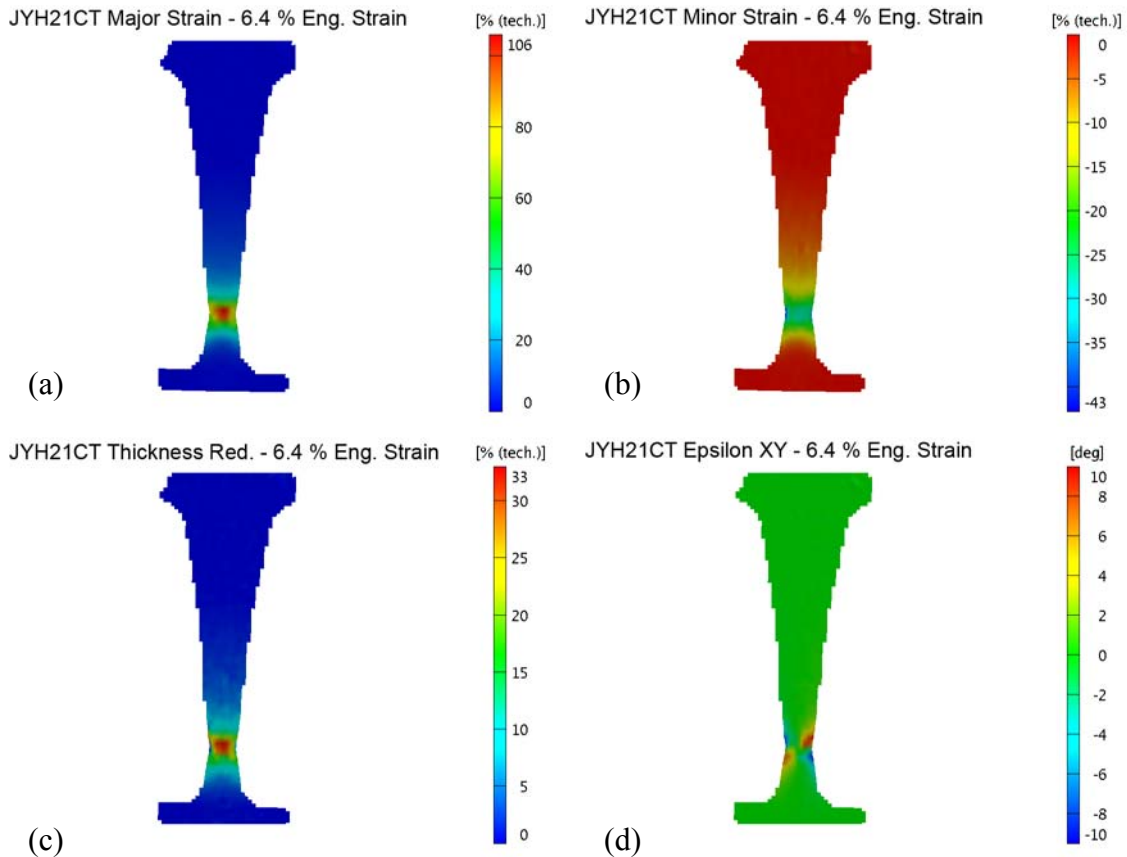


Fig 4.9a-d. Different strain components calculated by the Aramis software on a JYH21CT steel sample. a) Major strain (tensile direction); b) minor strain (in the direction of the width of the sample); c) thickness reduction; d) shear strain. The images show the strain right before fracture.

With Aramis it is possible to measure strains as a function of time at a certain point on the sample. Such a point is called a stage point. Aramis can also be used to show different strains through the whole length of the sample at a certain time. In Figure 4.10 one can see the different points and sections defined at the sample surface where strain is visualized, to be seen further in this paragraph. The sections in Figure 4.10 lie a millimeter apart and extend from clamp to clamp.

JYH21CT Major Strain - 6.4 % Eng. Strain

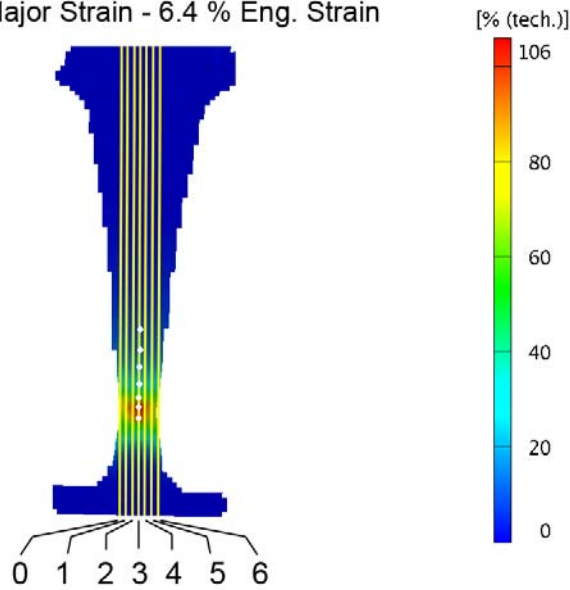


Fig 4.10. Sections (yellow) and stage points (white) on a surface model of a JYH21CT steel

Strain development near fracture

The results of the stage point measurement on JYH21CT steel can be found in Figure 4.11. The stage point in this figure is a point near the fracture area, the bottom point in Figure 4.10. The figure shows a strain rate of $1.1 \cdot 10^{-3} \text{ s}^{-1}$ the first 130 seconds. Roughly around 240 seconds the strain rate has become $9.5 \cdot 10^{-3} \text{ s}^{-1}$. Finally at 96% strain, fracture takes place.

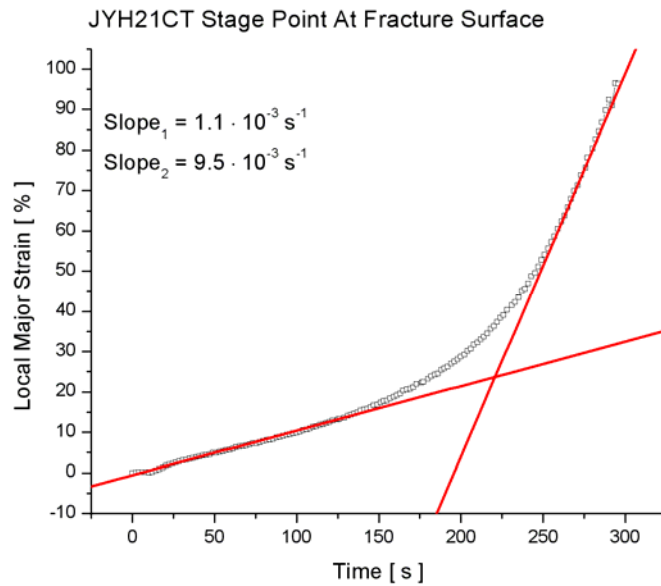


Fig 4.11. Strain development near the fracture area during a tensile test on JYH21CT steel. The macroscopic strain rate during this test was $2.2 \cdot 10^{-4} \text{ s}^{-1}$

Strain distribution near moment of fracture

The sections given in Figure 4.12 are the result of the same tensile test and sample as shown in Figure 4.10 and Figure 4.11. The origin of the graph is at the point at which the sample is fixed in the bottom machine clamp. Here the sample has zero displacement; the upper clamp is moved upwards during the experiment. All section graphs are based on sample images that are taken just before fracture.

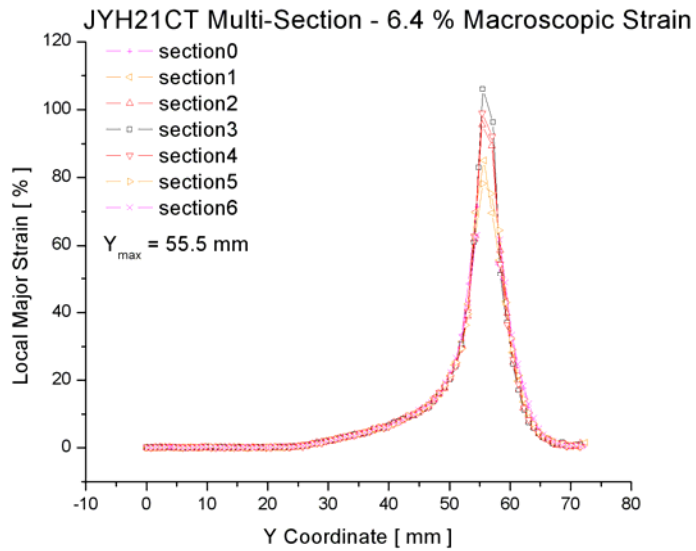


Fig 4.12. Strain distribution along the tensile direction of a JYH21CT steel sample shortly before failure. The sections are shown in Fig. 4.10.

The figure shows an equal distribution of local strain over the width of the sample, with exception of the area near the fracture. There the local major strain is about 70 % near the side (section 1 and 5) and 106 % in the middle of the sample (section 3). Section 0 and 6 don't contact the sample in the fracture area, but lie next to the sample.

Two regimes of strain behavior

When looking closer to the plots of the local major strains along the length of the sample right before fracture, one can see that the behavior can be approached by two linear regimes and an intermediate stadium. This is illustrated in Figure 4.13, where the major strain along the length of samples of both AISI410 and JYH21CT is shown, right before fracture. Far from the necked area of the sample, the strain increases only about 0.3-0.5 % mm⁻¹. However, coming closer to the fracture (starting about 10 mm from fracture), local strain increases up till 15-25 % mm⁻¹. In Figure 4.13 the y = 0 coordinate is at the fracture point. The sections are taken from the middle of the sample (section 3 of Figure 4.10).

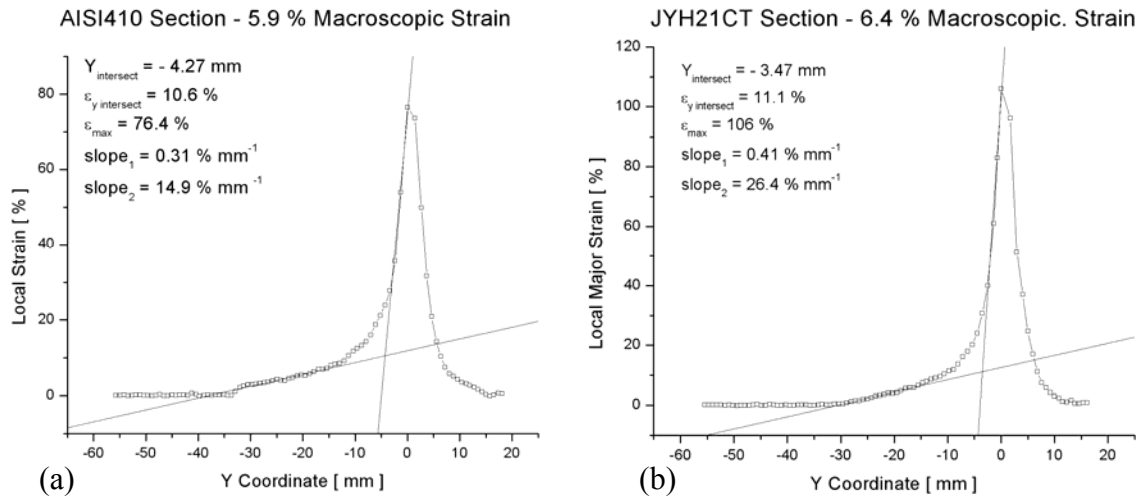


Fig 4.13 Sections from the AISI410 steel (a) and the JYH21CT steel (b) samples. The sections show local major strains across the length of the sample and are approached by two linear regimes and an intermediate stadium.

Strain distribution development

Another feature of the Aramis software is that it can create a diagram of strain distributions at different times. In Figure 4.14 such a diagram is presented. At certain macroscopic strains the local strains have been measured along the section of a JYH21CT sample, giving development of the strain distribution.

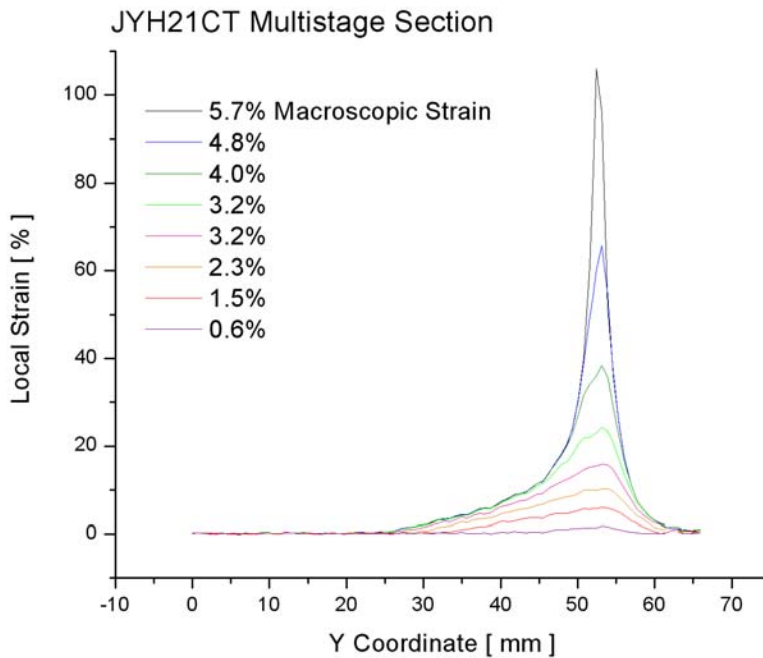


Fig. 4.14
Development of
strain distributions
at certain
macroscopic strain
in a JYH21CT steel
sample along section
3.

True stress-strain curves at different sample points

Using the output voltage of the tensile machine - which is proportional to the load on the sample - and the strain values calculated by the Aramis system, one can create a true stress-strain curve for the tested material. The local minor strain and thickness reduction are both used to correct the area of the smallest cross-section at the critical point. Different stage points in areas of the sample under large strains (see Figure 4.10) have been taken to create these curves. The results are presented in Figure 4.15a and b.

Figure 4.15a shows behavior which is similar to what can be seen in the engineering stress-strain curve of Figure 4.7a. The AISI410 steel has a typical distinctive elastic-plastic transition at about 2.0-2.5%. The upper yield point is determined to be about 360 MPa. The stress reaches a maximum of about 510 MPa when strain increases, followed by a slight decrease in stress. At stage points away from the sample fracture deformation stops after a certain strain value, while the stress drops to zero.

Figure 4.15b shows no yield points for the JYH21CT steel, as in Figure 4.7a. The yield strength is determined to be 340 MPa at 0.46% strain. The stress in this figure does not decline after a certain point but keeps rising, in contrast with the engineering stress-strain curves of both steels as well as the true stress-strain curve of AISI410. This makes Figure 4.15b a very typical true stress-strain diagram.

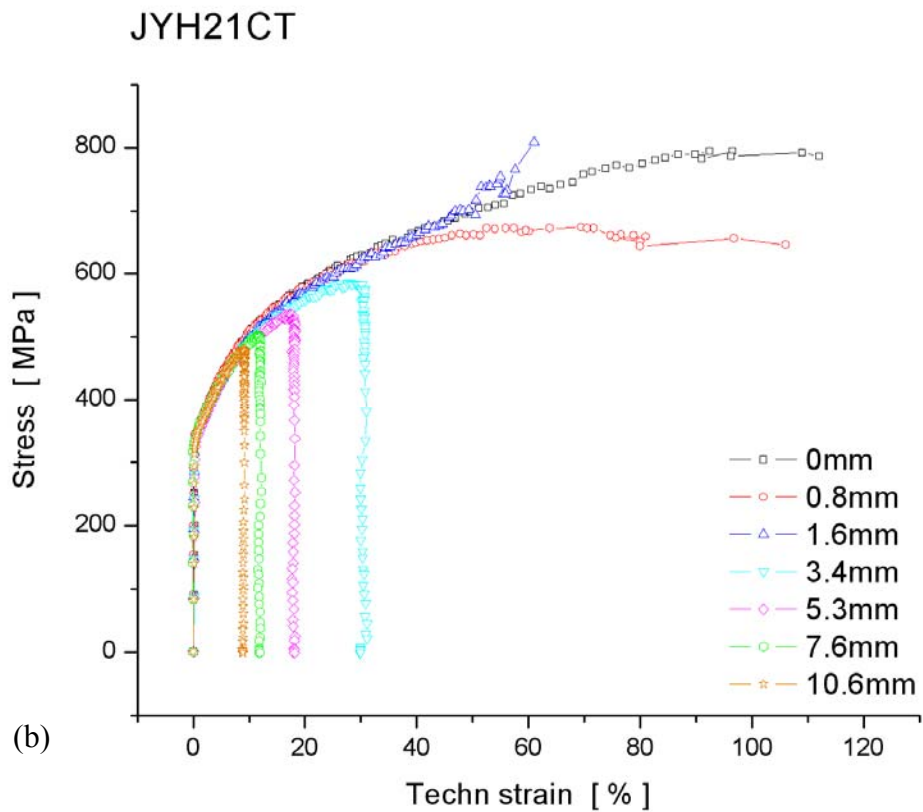
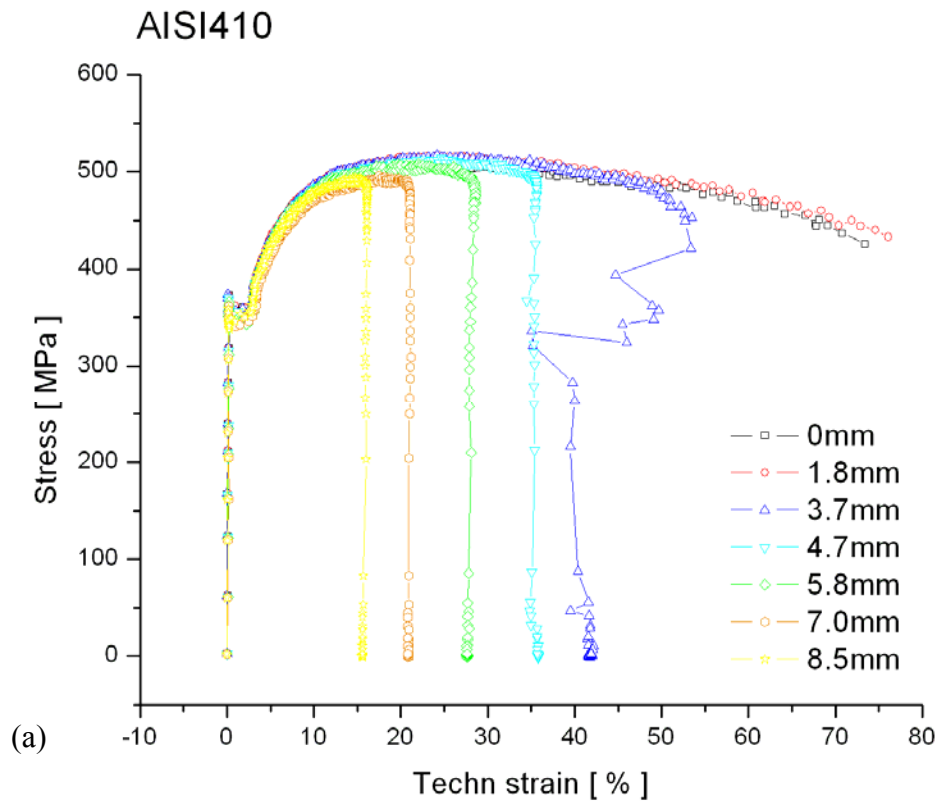


Figure 4.15 True stress-strain curves for AISI410 (a) and JYH21CT (b) in different points in the tensile test samples. The distances are measured from the point where fracture occurs.

4.4 Fractography

Macro of fracture plane

Figure 4.16 shows a comparison of the fracture surfaces of AISI 410 and JYH21CT steel samples after failure in the tensile experiment.

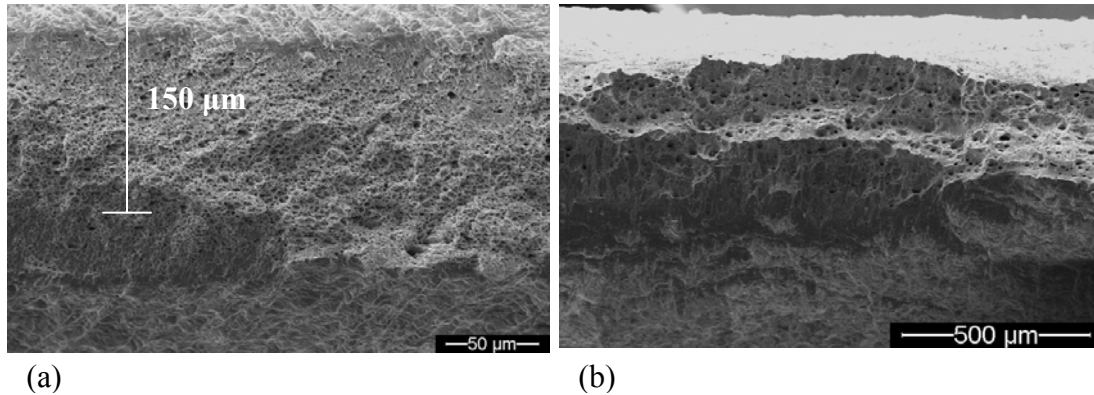


Fig 4.16 SEM observation of the fracture surface after the tensile test on an (a) AISI 410 and (b) JYH21CT steel sample

The AISI 410 sample was 0.5 mm thick before the test and the fracture plane was, macroscopically, perpendicular to the sample surface and approximately 45° inclined to the tensile direction. Figure 4.16a shows a view to this fracture plane from the tensile direction. The final sample thickness in the fractured necking area is 150 μm , which means that there is a thickness reduction of about 330%.

The fracture surface of the AISI 410 steel shows a typical ductile type of fracture with dimples which are distributed homogeneously over the whole fracture surface. On the other side, Figure 4.16b shows the ductile fracture observation on the tensile tested JYH21CT steel sample. Macroscopically, the fracture surface is oriented approximately 45° with respect to the tensile direction and to the surface of the sample. The dimples are not distributed homogeneously over the whole fracture surface but they are denser at the top part of Figure 4.16b.

Dimple size and distribution

The Figures 4.17 focuses more on the observation of the distribution in dimple size on the fracture surface of the steels examined.

Figure 4.17a shows that the dimples on the fracture surface of the AISI 410 steel are relatively equally sized, with a maximum size of about 3 μm .

The fracture surface of JYH21CT steel shows a large difference in dimple size (Figure

4.17b). The dimples lying at the top of the image are about 25 μm in diameter and the dimples in the shear region of the fracture surface, at the bottom of the image, show

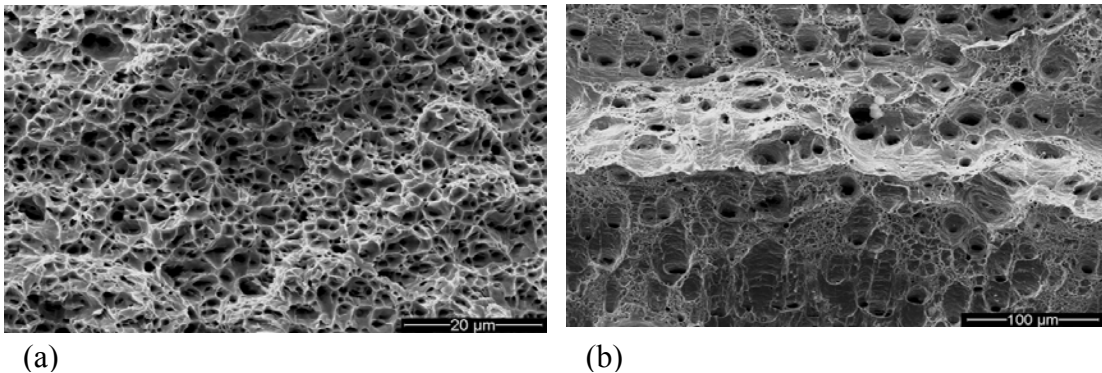


Fig 4.17 SEM images which focus on the distribution in dimple size on the fracture surfaces of samples of (a) AISI 410 and (b) JYH21CT steel after the tensile experiment

that they can have a depth up to 70 μm . But there are also very fine dimples observed between the larger dimples, with a diameter of about 1 μm and less.

Figure 4.18 shows a detail of some dimples in the shear area at the fracture surface of the tensile tested JYH21CT steel.

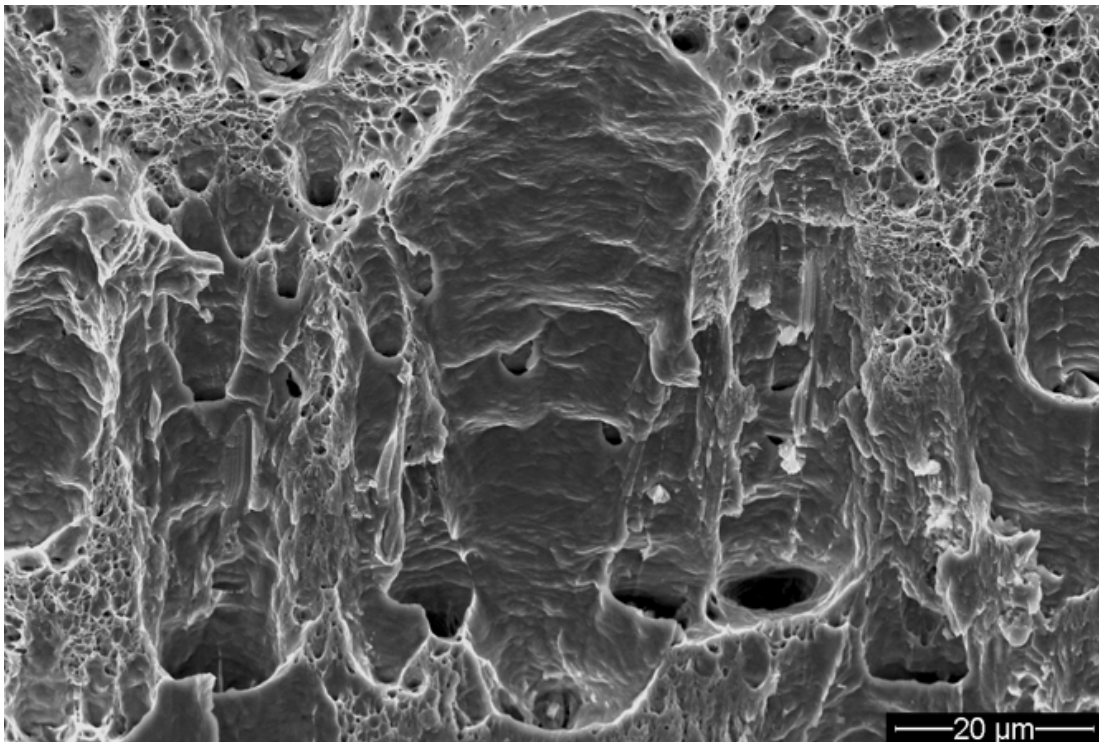


Fig 4.18 SEM image of dimples in the shear area of the fracture surface of JYH21CT steel. At the bottom of large dimples inclusions are observed, as well as scratches on the dimple walls.

From this image the width and shear length of the large dimple can be determined, which are about 25 μm and 70 μm respectively. Also, the finer dimples on the sides of the larger ones can be distinguished clearly on this image.

On the bottom of almost each large dimple a rectangular inclusion particle can be seen, which presumably initiates the forming of that dimple. These hard inclusions are either sitting at the bottom of the dimple or they are moving during the fracture, creating scratches at the dimple walls as Figure 4.18 clearly demonstrates.

Dimple initiation

A closer look at the dimples on the fracture surfaces of the tensile tested AISI 410 and JYH21CT steel is shown in Figure 4.19.

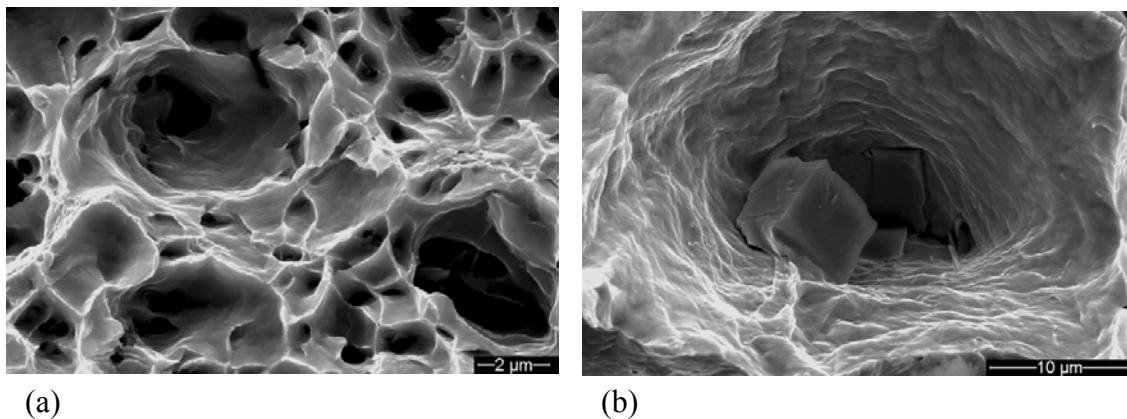


Fig 4.19 SEM image showing a closer look at the dimples on the fracture surface of the tensile tested steels (a) AISI 410 and JYH21CT

Inclusions are found in almost every dimple on the fracture surface of the JYH21CT steel, mostly at the bottom, like Figure 4.19b shows. The inclusions are expected to be responsible for the forming of the large dimples of the JYH21CT steel. One might expect to find some sort of inclusions in the AISI 410 case, too. But as Figure 4.19a demonstrates, no inclusion or impurity can be found in and around the dimples on the fracture surface of the AISI 410 steel.

From these SEM observations, the size of the inclusions in the JYH21CT steel is found to be about 2-5 μm .

4.5 Voids in JYH21CT

SEM Observations

A measurement of the number of voids with respect to the distance from the fracture surface has been performed on cross section A (see Figure 3.3) of a JYH21CT steel sample after tensile testing. Also the length of the voids in tensile direction has been measured, assuming that this length is a good indication of void size. This can be seen in Figure 4.20a, which shows two typical voids in the tested sample. One can see clearly that void initiation is happening at the left or right of the inclusions and not above or below. Fig. 4.20b shows void nucleation on both sides of the inclusions. The figures also show how void length is determined. Inclusions are considered as a part of the void, since one cannot know all dimensions of a void, i.e. the material that is removed by polishing and the structure underlying the cross-section surface. The inclusion length varies from about 2 μm till 4 μm . Voids smaller than 2.5 μm without a presence of inclusions are not taken in account, as these are most likely created by inclusions that have been removed by polishing, without any void initiation by strain. Also some square or rectangular voids that are larger than 2.5 μm are most likely not created by strain and therefore ignored (see Figure 4.20c).

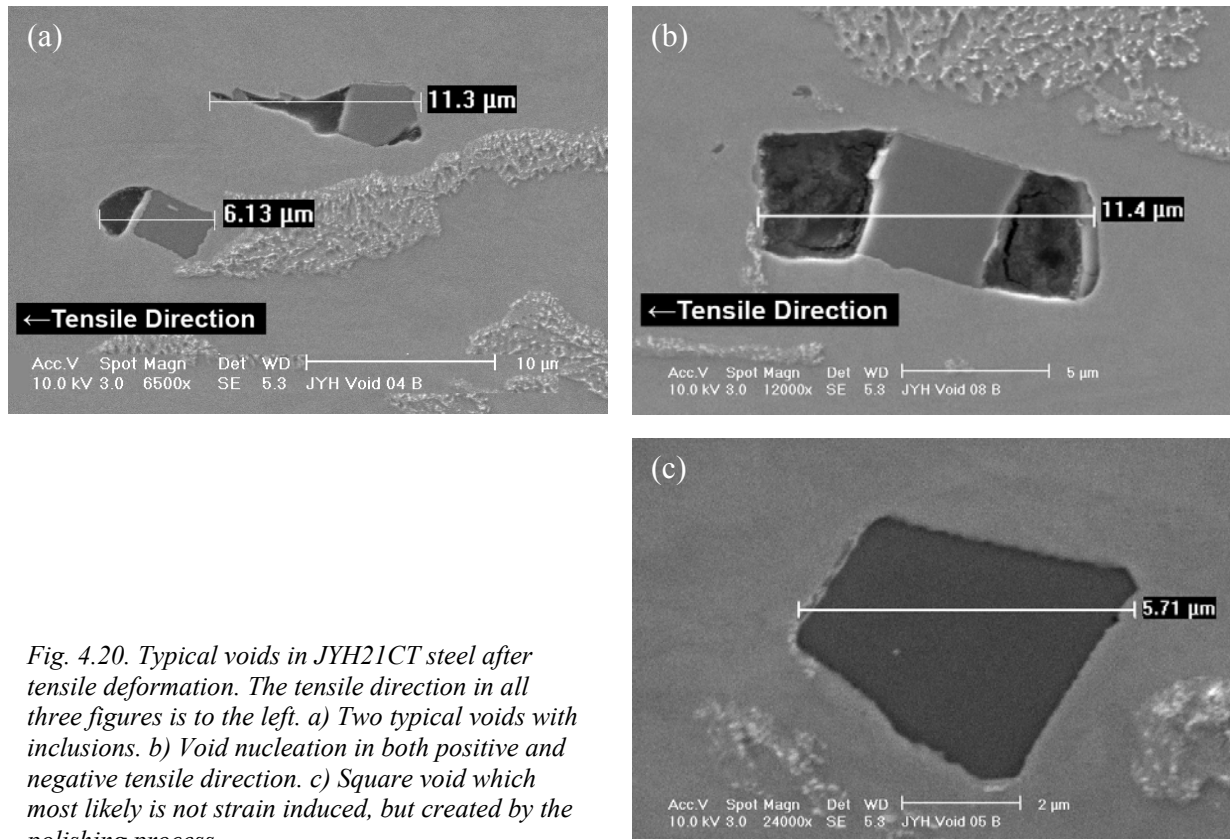


Fig. 4.20. Typical voids in JYH21CT steel after tensile deformation. The tensile direction in all three figures is to the left. a) Two typical voids with inclusions. b) Void nucleation in both positive and negative tensile direction. c) Square void which most likely is not strain induced, but created by the polishing process.

Statistics

In Fig. 4.21 the void density in different strain regions on a tensile tested JYH21CT sample is given. About 180 voids in total were present on the fractured sample. This number is somewhat too low to give statistically accurate results, but a decrease of void density with a distance from fracture surface can clearly be observed in the figure.

Figure 4.22 shows the average length of voids in the same regions as in the previous figure. It suggests that void length is independent of strain region, although there seems to be a minor increase in the regions above higher strain regions.

Though more statistics are needed, an assumption from both figures can be made. Void mechanisms can be roughly divided into two regions. The first is void initiation at strains below 66%, concluded from the increase in density. Second is void growth with strains from 66% till failure, while density remains at the same level.

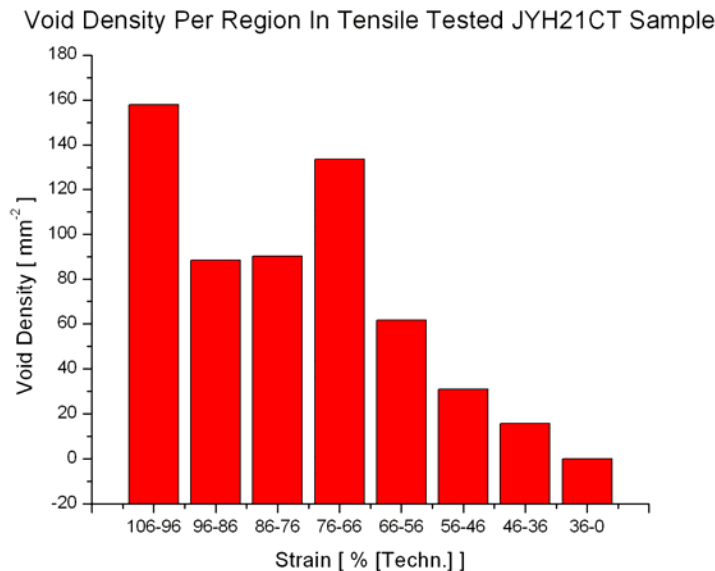
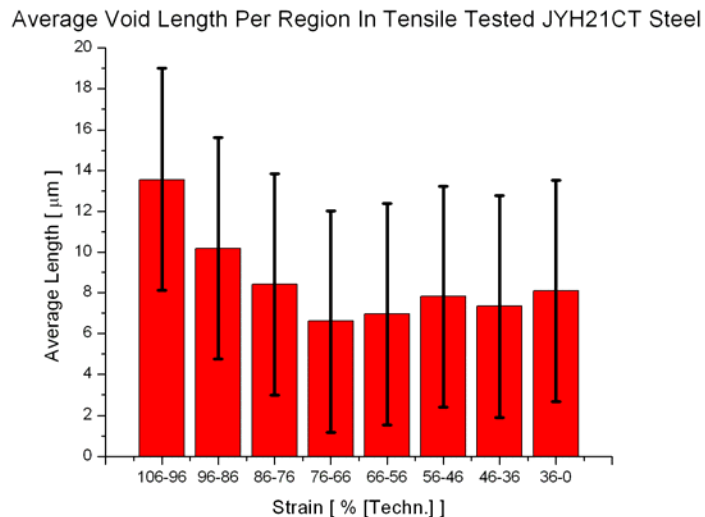


Fig 4.21 Void density in regions having a certain strain range on a JYH21CT sample.

Fig.4.22 Average void length in strain regions on a JYH21CT sample.



4.6 OM observations

Macro view of JYH-steel sample 1

Figure 4.23 shows an overall view of the highly strained area of a cross-section of a tensile tested JYH21CT steel sample. The part shown is part a; the intersection of the sample taken parallel to the tensile direction (see: 'Sample cuts and preparation'). From the Aramis experiment it follows that the final tensile strain near the fracture surface was about 100%, while the tensile strain at the right of the image, at 4 mm from the fracture surface, was about 30%.

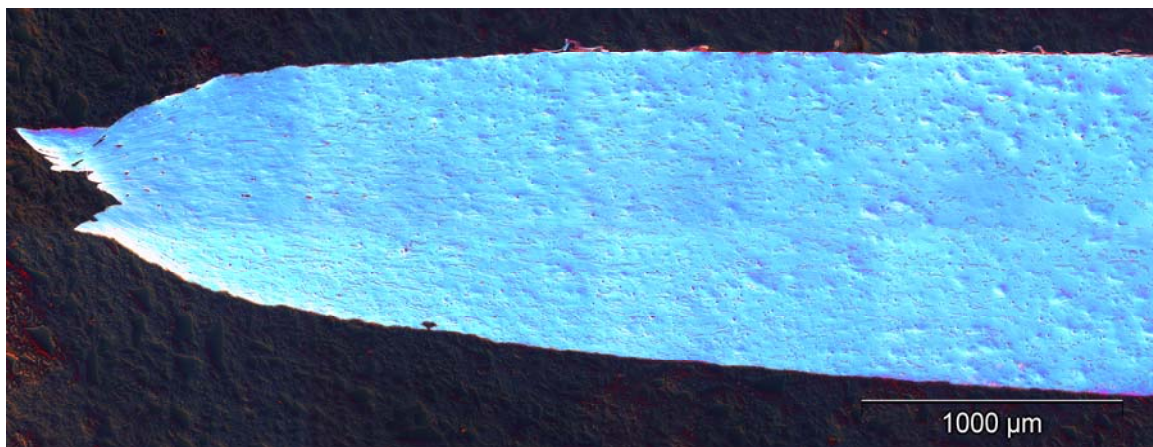


Fig 4.23 Stitching of images has produced this macro view of the intersection parallel to the tensile direction of a tensile tested JYH21CT steel sample on the optical microscope

This broad image shows clearly the necking which precedes the final fracture. This thickness reduction is 10% at 4 mm from the fracture surface. The Aramis experiment confirmed that the thickness reduction at 4mm from the fracture surface is indeed 10%.

There is more relief close to the fracture surface than on the right side of the image in the less strained area. Grains which show a rough surface, even after the polishing procedure, are showing up more and more looking from the right to the left of the image. Not only the density of these grains becomes higher with increasing strain, they are also elongated and they seem to orient themselves towards the point or area of fracture. This change in grain shape and the orientation of this shape will be investigated further in the OIM analysis.

The image is also showing dark spots in the fracture surface neighborhood. These are voids and are almost always accompanied by the presence of inclusions. Although the voids do not appear in large numbers, their distribution over the sample has been examined with an SEM investigation.

Detailed OM images from different strain areas

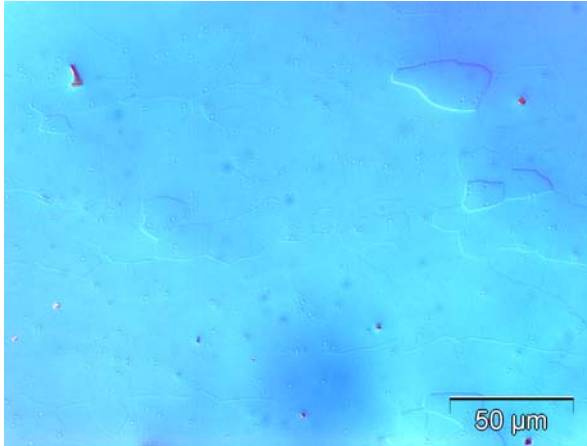
Details of the features that are deduced from the macro view of the tensile tested JYH21CT steel sample are shown in the sequence of images of Figure 4.24. Each picture is taken at the same magnification and from the center of the sample. The strains are deduced from the Aramis experiment results.

Figure 4.24a shows what the surface of the intersection looks like when there is (almost) no strain. A few grains and inclusions are visible and the surface is smooth. At 22 % of tensile strain (Figure 4.24b), a few grains with a more rough surface are visible. Evidently, these rough-surface grains are formed by the larger amount of strain in this area of the material. The reaction of these grains on the polishing procedure causes a relief which is visible on their surface.

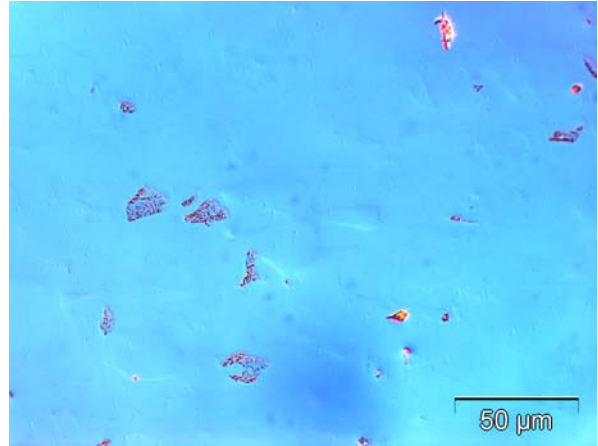
Figure 4.24c shows that at a higher amount of strain more of these grains are formed and that they tend to elongate in the tensile direction. At even higher strains, like in Figure 4.24d, the density of the rough-surface grains hasn't increased visibly, but they are more elongated and therefore thinner.

Figure 4.24e shows large areas filled with rough-surface grains which are also longer than at areas of lower strains. A void is visible as a red scratch in this image. A part of an inclusion is visible in the left corner of the void, recognizable by its straight sides at a 90° angle.

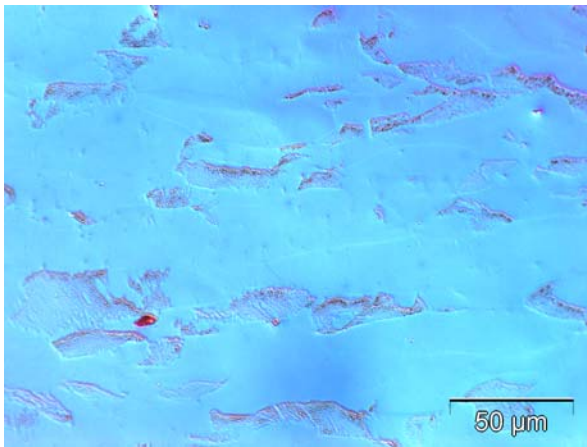
In the high strained area shown in Figure 4.24f the rough-surface grains are even more elongated than before. Just right of the center of the image, an inclusion is visible with a drop-shaped void next to it.



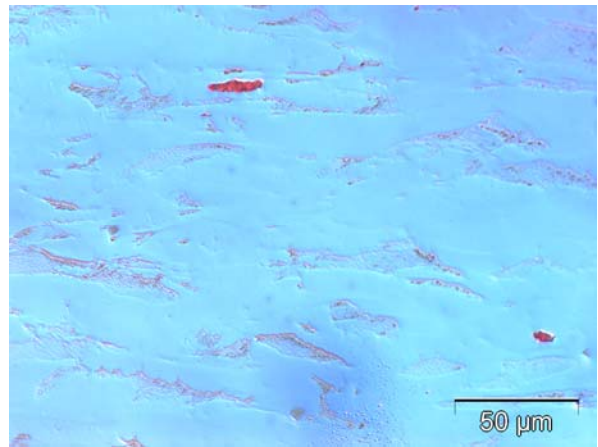
(a) At 20 mm from FS – 4.2% tensile strain



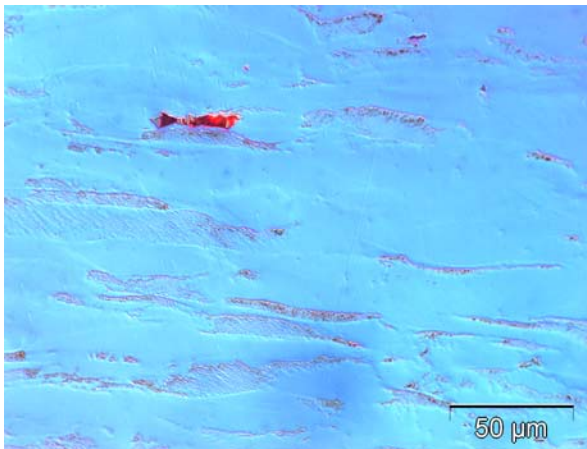
(b) At 5 mm from FS - 24 % tensile strain



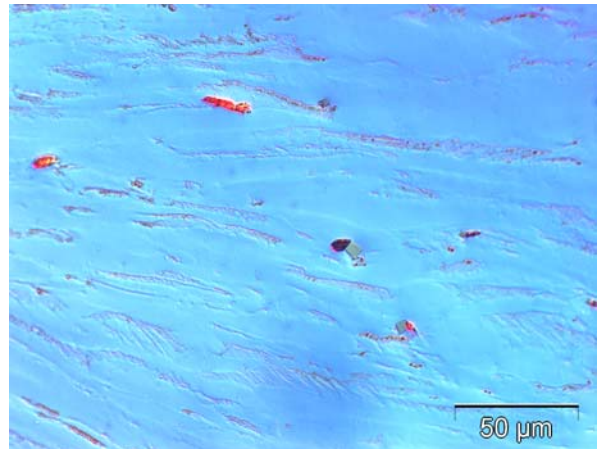
(c) At 2 mm from FS - 50 % tensile strain



(d) At 1 mm from FS - 75 % tensile strain



(e) At 0,5 mm from FS - 85 % tensile strain



(f) At 0,1 mm from FS - 100 % tensile strain

Figure 4.24 Optical microscope detail images at areas with different strains of the same sample as in Figure 4.23 at a magnification of 50. (FS = fracture surface)

Observations bending samples and hardness measurement

Figure 4.25 shows an optical microscopic image of a JYH21CT sample, which has been bent under high strain rate, with a bending radius of 1.5mm. The photo shows a few inclusions, but no voids appear. The maximum strain is estimated about -30% in the compression and 30% in the tensile area. Furthermore some hardness measurements have been performed, on both tensile and compression area and on the undeformed area. The results can be found in Table 4.3. The undeformed area clearly has a lower hardness number then the areas under large deformation. The three bigger dots indicated in Figure 4.25 are imprints of these hardness measurements.

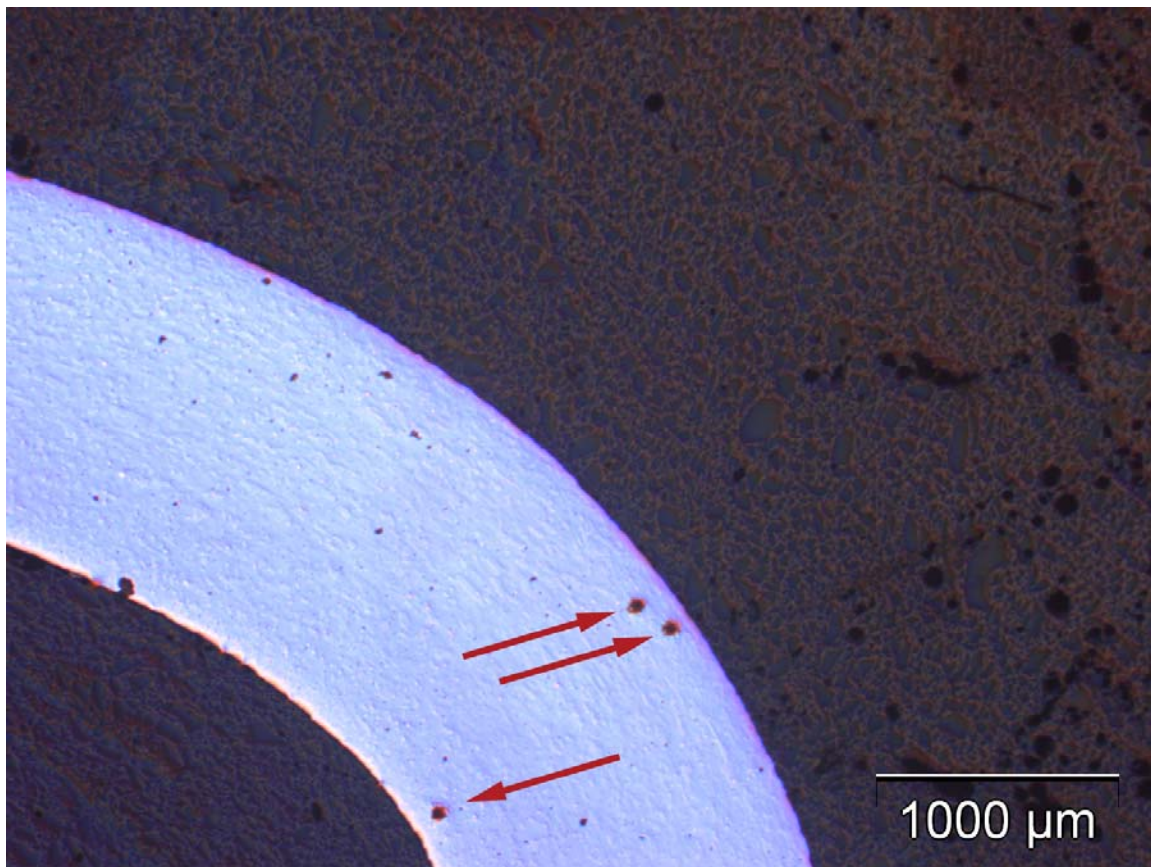


Fig 4.25 JYH21CT steel sample bended under high strain rate. Hardness Measurements have been performed at the points indicated with an arrow.

	Tensile area	Compression area	Undeformed area
Hardness (HV0.4)	236	231	149

Table 4.3. Vickers hardness testing on bent JYH21CT steel

4.7 OIM observations

Parameters to quantify damage by strain

Eight OIM scans have been performed on the intersection of a sample of JYH21CT steel after the tensile experiment, at various distances from the fracture surface. Five scans have been performed on the surface of the same sample.

The scans in the bulk of the sample consist of 629186 points with a step size of 0.25 μm . They contain 100 grains on average. The scans on the surface consist of 39497 points with step size 1 μm . They contain 80 grains on average. They are both performed on an area of 100x340 μm .

This paragraph presents the analysis that has been performed on different features of these scans to try to find a good parameter to quantify damage in the tensile tested samples. The strain at the location of the scans is known from the Aramis experiment. The TSL OIM Analysis 4.6 software has been used to evaluate a number of parameters, namely grain diameter, average misorientation spread, misorientation gradient, grain shape aspect ratio and grain shape orientation. The details of the methods used to calculate these parameters are described in the Appendix.

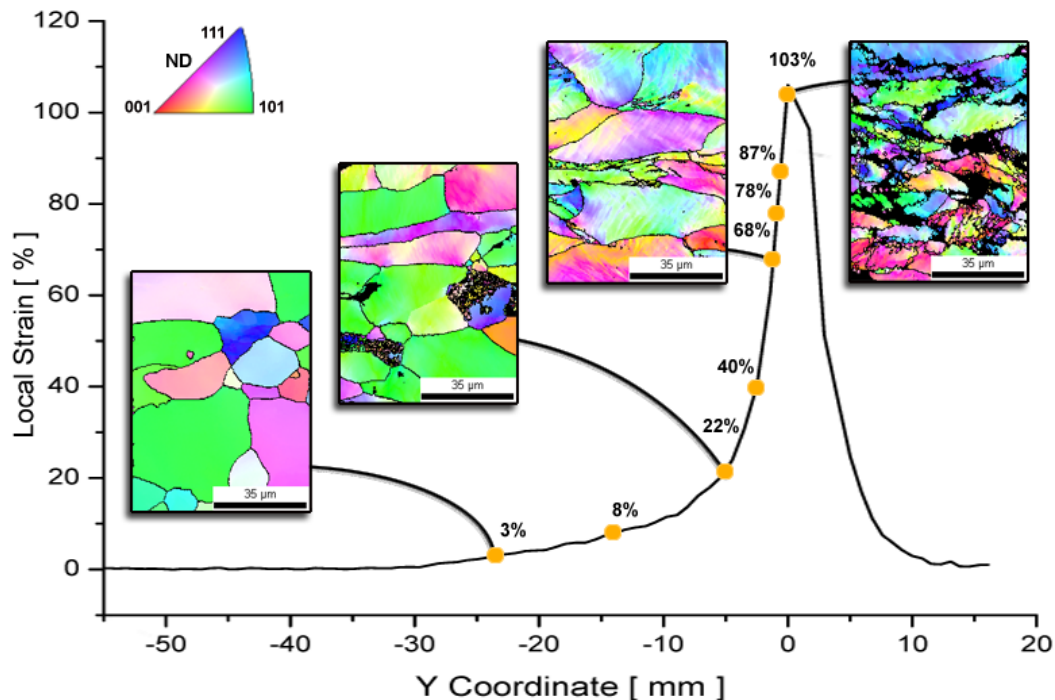


Fig 4.26 Graph of the strain in a tensile tested JYH21CT sample as a function of the distance from the fracture surface and parts of OIM scans in IPF representation performed on the cross-section through the thickness of a sample of JYH21CT on several areas with different strains.

Figure 4.26 shows parts of four scans in the bulk of the sample and their position on the distance-to-strain curve. The black lines in the scans are grain boundaries, which are drawn between each 2 points with orientations differing more than 5° . The black areas are non-indexable points.

The scan at 3% of strain shows uniform colored grains, indicating that all points within the grain have the same orientation. At 22% of strain, the scan shows some grains containing a color gradient, which indicates misorientation within the grain. Also, the grains are a bit elongated in the tensile direction. This effect is even larger at 68% of strain. There is also much more misorientation within the grains visible in this scan. In the area of 100% of strain the grains are even more deformed. This can be seen from all the different colors within a grain and the smaller size of the grains. The best parameter to quantify the changes in the microstructure that these scans show, seems to be the misorientation angle. Some more evidence on the increase of misorientation within a grain during the loading is given by Figure 4.27a and b. These are inverse pole figures of the tensile tested JYH21CT steel sample at 0% and 22% of

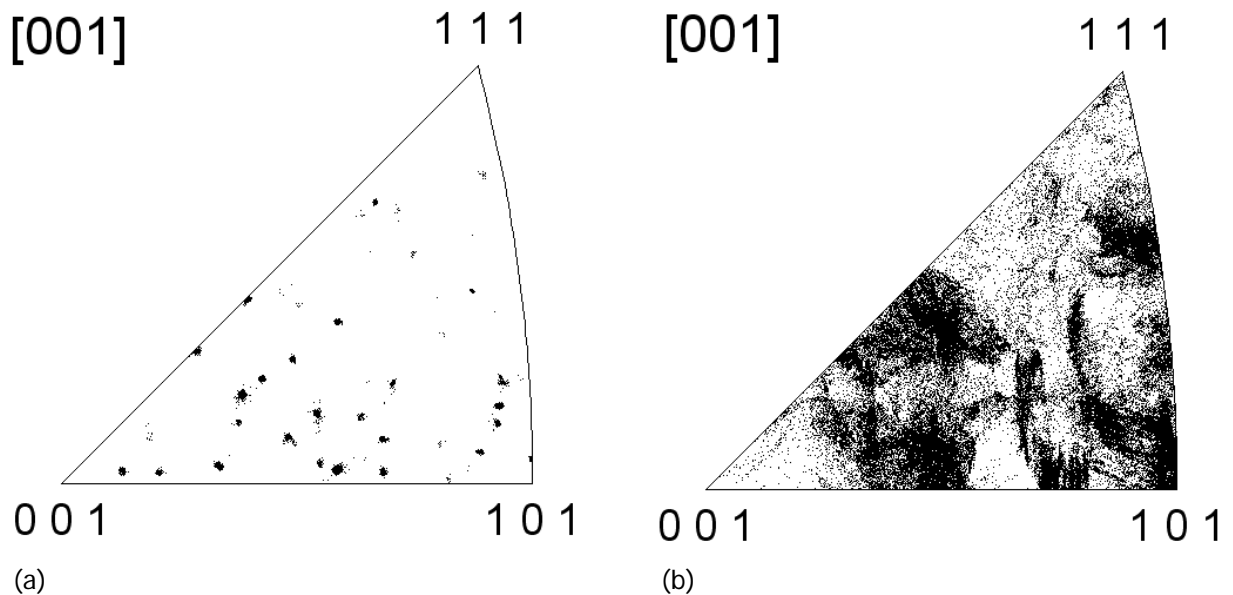


Fig 4.27 Inverse pole figures showing the orientation of grains in the JYH21CT steel sample with respect to the $[001]$ direction for a) 0% of strain and b) 22% of strain.

strain respectively.

In Figure 4.27a, at zero deformation, individual grains can clearly be recognized as a burst of small dots. Each burst represents a grain in which all points have almost the same orientation. In the inverse pole figure at 22% of strain (Figure 4.27b) it is impossible to distinguish one grain from another. The wide distribution of dots indicates that the grains contain points with a lot of different orientations, thus implicating an increase of misorientation angle for higher strains.

Average grain orientation spread

To quantify the misorientation within a grain, the grain orientation spread is used. This is the average of the misorientation angle of all points in a grain from the central orientation of that grain. In Figure 4.28a, b and c the distribution of the grain orientation spread is shown for 0%, 40% and 100% of strain respectively, measured on an array of at least 80 grains. These distributions can all be fitted with a log-normal distribution from which the mean value and the standard deviation is calculated. This mean value is taken as the Average Grain Orientation Spread (AGOS) for a certain strain and is given in the figures.

The shape of the distribution is almost equal for all strains, there is only a shift in the mean value and a slightly larger standard deviation for increasing strain.

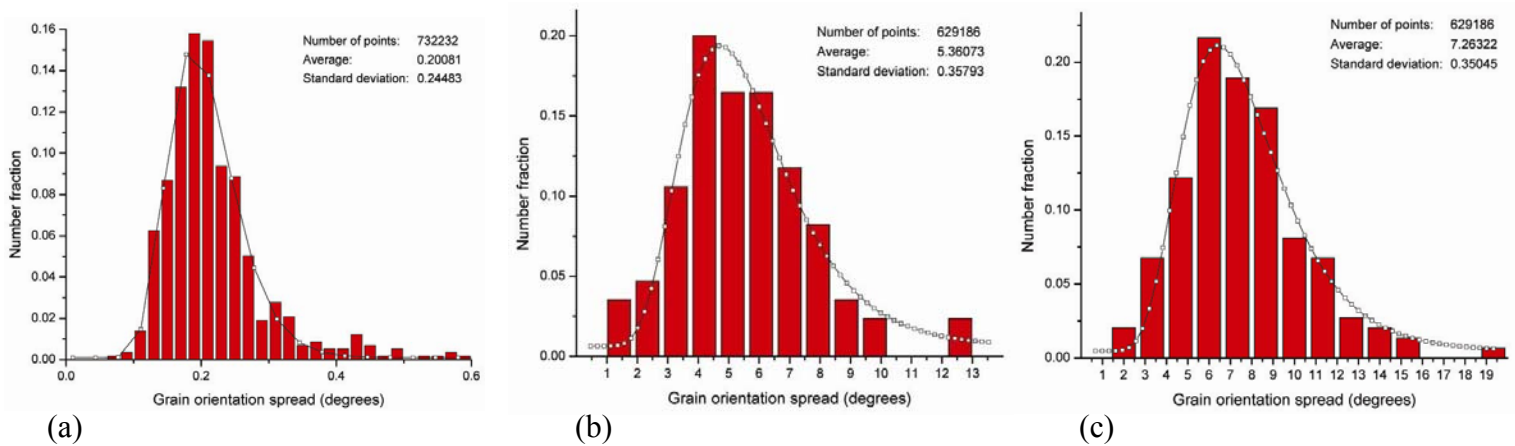


Fig 4.28 The distribution of the grain orientation spread of the bulk of JYH21CT steel fitted with a log-normal function for a) 0%, b) 40% and c) 100% of strain.

The AGOS values and their standard deviations are plotted against the strain in Fig 4.29. This figure shows these values measured on OIM scans on the intersection through the thickness of the sample. This gives the AGOS in the bulk of the sample. It also shows the AGOS on the free surface of the sample.

The graphs show a striking resemblance for the AGOS on the surface and in the bulk between 0% and 22% of strain. In this region the curves are both linear. They also show a linear behaviour above

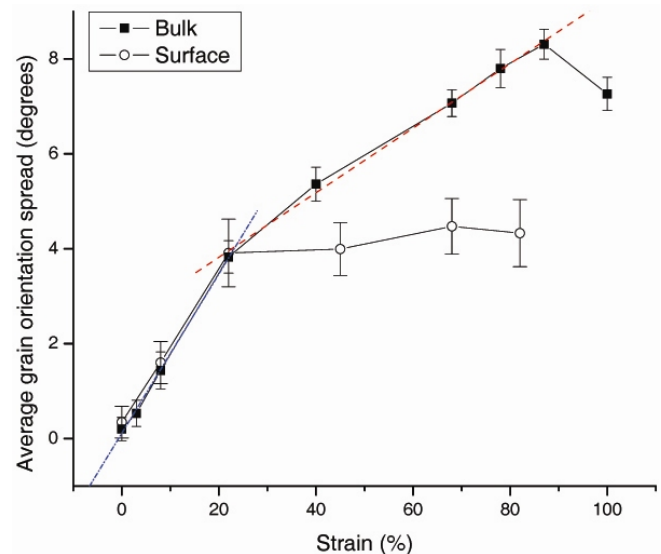


Fig 4.29 Average grain orientation spread measured as a function of local strain at the free surface and in the bulk of tensile tested JYH21CT steel

22% but both with a different slope. Judging from the curve belonging to the surface AGOS, there is no contribution of the strain to the AGOS in this region. The slopes of both curves in the two regions are given in Table 4.4. The numbers in this table emphasize the equal slopes of the curves in the region of 0% to 20% strain. The errors in the results for the surface are relatively large.

	0%-22% Strain		> 20% Strain	
	Starting point (deg)	Slope (deg/%)	Starting point(deg)	Slope (deg/%)
Bulk	$0,11 \pm 0,06$	$0,168 \pm 0,005$	$2,46 \pm 0,16$	$0,068 \pm 0,002$
Surface	$0,34 \pm 0,31$	$0,161 \pm 0,035$	$3,66 \pm 0,88$	$0,001 \pm 0,015$

Table 4.4 Starting points and slopes for the linear fits of two regions in the curves of Figure 4.26 of tensile tested JYH21CT steel.

Average misorientation gradient

Another method to quantify the amount of misorientation within grains is the misorientation gradient. This is the average of the misorientation between all neighboring pairs of points in a grain. Figure 4.30 shows the average of this parameter over all grains for scans in the bulk and on the surface of JYH21CT steel. The misorientation gradient distribution in the bulk, for 40% of strain, is fitted with a log-normal distribution. The standard deviation from this fit is a measure of the error and is given in the figure. The same is done on the surface for 45% of strain. Both curves show a slight nod at 22% of strain, after which the slopes of the curves are almost equal. The last points on the curves, at high strain, seem to be inaccurate measurements.

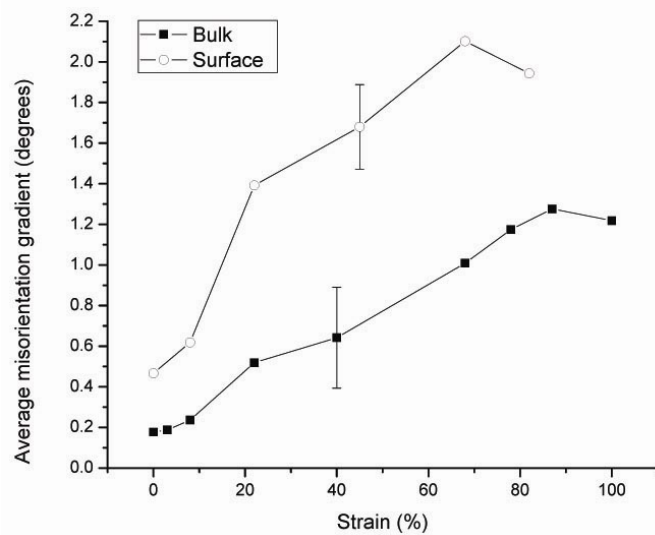


Fig 4.30 Average misorientation gradient against strain for both the bulk and the surface of tensile tested JYH21CT steel.

Average grain shape aspect ratio

By approximating the grain shape with an ellipse a quantification of the elongation of the grains can be given. This is done by calculating the aspect ratio between the long and the short axis of the ellipse. Figure 4.31 shows the results of this analysis method on the bulk and on the surface of the sample. The other two curves are calculated by two simplified models. The blue dashed curve shows the aspect ratio assuming that the grain can be represented by an ellipse whose area is fixed. The major strain is taken from the Aramis experiment and assumed to act solely on the long axis of the ellipse. By these two constraints, the short axis of the ellipse and thus the aspect ratio can be calculated as a function of local major strain. All measurements lie above this model, so it is overestimating the grain elongation. The second model uses the major strain and the thickness reduction, both calculated from the Aramis experiment. The major strain is used to calculate the length of the long axis, the thickness reduction determines the length of the short axis. The red dashed curve in Figure 4.31 shows the aspect ratio approximated by this model. It is seen from the figure that it underestimates the actual effect of elongation of the grains.

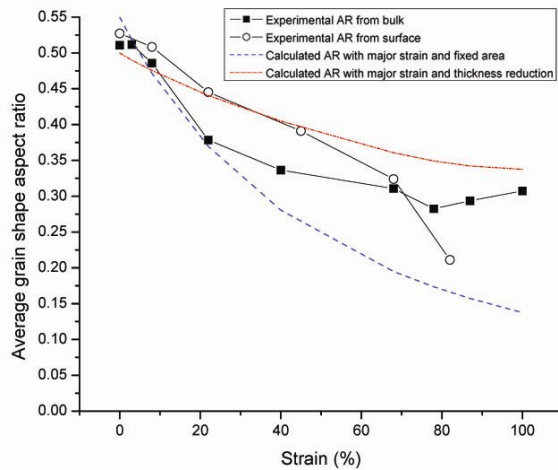


Fig 4.31 Average grain shape aspect ratio against strain for both the bulk and the surface of JYH21CT with curves calculated from simplified models

Grain shape orientation

From OM observations it is seen that for increasing strain, the grains seem to orient itself along the tensile direction. Therefore the Grain Shape Orientation has been examined. To calculate this parameter, the grain shape is again approximated with an ellipse. The GOS is the angle between the long axis of the ellipse and the tensile direction. However, in our research, the grain shape orientation didn't show a good correlation with the strain.

5. Discussion

A similar grain size and grain shape aspect ratio is observed at different cuts of the JYH21CT steel. This means that from point of view of grain size and shape, the rolling texture was almost fully removed by soft annealing of the material. The orientation texture found on the surface of both AISI 410 and JYH21CT can be described by two preferred crystal orientations:

- The crystal $\langle 111 \rangle$ directions are preferably parallel to the ND direction of the sample.
- The crystal $\langle 001 \rangle$ directions are preferably parallel to the transverse direction with the (001) plane inclined 45° to the normal direction of the sample.

However, a substantial difference in grain size of AISI 410 and JYH21CT detected by OIM observations may lead to a difference in high temperature mechanical properties.

Void initiation during plastic deformation of JYH21CT only happens on the boundary interface between the Fe-Cr matrix and the TiN inclusions. As strain increases, voids initiate on TiN facets being oriented perpendicularly to tensile direction and having low adhesion to the matrix. The TiN inclusions are formed probably before the final melt solidification, they are not coherent with matrix and they have low adhesion to the matrix.

The true stress-strain curves presented in paragraph 4.3 (Figure 4.15) are calculated for few points with a different distance from the fracture surface. At some points, defined a few millimeters away from the fracture surface, the Aramis software can evaluate strain even when failure process starts, since local deformation stops at a certain moment during the tensile test. In the necking area the local deformation after failure is too high to be measured by DIC. Thus in Figure 4.15, we can only see the unloading of the sample after failure in points that aren't defined near the fracture surface.

Figure 4.15a shows the true stress-strain curve for AISI410 steel. In this figure the local stress doesn't continue to increase with strain, as is the case in figure 4.15b, but decreases after about 25% of strain. An explanation for this is the 45° fracture plane angle with the tensile direction due to shear. Stress is calculated with the cross-section area in the necking region, approximated by a single facet behavior. This approximation is less accurate with such a fracture plane angle due to a relative larger shear, as is the case with thin samples such as AISI410 samples used in this study.

When looking at figure 4.11 one can distinguish two regions of local strain rate. The first local strain rate region is a consequence of the sample geometry and macroscopic strain rate. The sample shape dictates that strain localizes in the narrow area, therefore local strain rate there must be higher than the macroscopic strain rate, in our case by a factor 5. The second strain rate region is mainly depending on the necking process controlled by material properties, e.g. hardening, ductility and presence of inclusions and voids.

The inclusions in the JYH21CT steel are found to be non-stoichiometric titanium nitrides. Titanium is usually added to low-carbon steels to prevent them from becoming brittle by collecting nitrogen from the melt.

The fracture surface of JYH21CT shows two distinctive sizes of dimples. The big dimples are the remainder of the voids that are formed by the TiN inclusions in this steel which act as nucleation sites. These voids are formed during the tensile experiment when the necking begins and the local strain increases. Fracture happens when these voids grow as big that they all coalesce. [6] At this last moment of the failure, the small dimples are formed to fracture the material at places where no inclusions exist. These small dimples are similar in size to the dimples that are found on the fracture surface of AISI 410 steel

The Vickers hardness of titanium nitride is about 2500 HV40. [4] The hardness of JYH21CT steel was measured in strained and unstrained areas. In the tensile area of the bent sample, which is approximately at 30% of strain, the Vickers hardness is about 230 HV40. From this big difference in hardness it is obvious that the Ti-inclusions are able to scratch the dimple walls as is observed on the fracture surface (see Fig. 4.18).

Two stages of damage accumulation by voids have been observed. The first is a void initiation stage, the second is void growth. Damage characterization by void statistics however does not give distinctive results due to a low void density on the investigated surface. To obtain statistically more correct results more data should be obtained by further investigation of voids, for instance by investigating a larger number of tensile samples, or by quantitative fractographic observations.

The average grain orientation spread (AGOS) measured by OIM on highly deformed surfaces shows two linear regimes. The first is for strain smaller than 20% where the bulk and the free surface grains show the same dependence of the AGOS with respect to strain. In the second regime, above 20% of strain, the AGOS in the bulk grains keeps growing but with a lower speed as in the first regime. The AGOS in

the surface grains does not grow anymore in the second regime. This difference can be explained by considering that the pure shear deformation (slip occurs on certain slip systems) does not contribute to the misorientation angle. In the bulk of the material, every grain is surrounded by other grains. Therefore, slip can barely occur and a rotation between parts of the grain is needed to let deformation happen. This causes misorientation within a grain. As the grains on the surface are free on one side, they are able to deform by a certain amount of slip. Therefore, there is no misorientation needed and so the AGOS does not grow anymore above 20% of strain. Because surface grains are still attached to other grains they do not have all freedom to move. This can explain the fact that there is a development of misorientation in the first region.

The errors in the results for the AGOS on the free surface are relatively larger than the errors in the AGOS in the bulk. The scans on the surface contain a lot less points than the scans in the bulk, so the distribution of the AGOS for these scans is wider. This causes a bigger standard deviation.

The linear behaviour of the grain orientation spread is also found in a study done by Kamaya et al. [5] They used several different microscopes, electron guns, spot sizes and step sizes for observations on 304SS steel which is strained up to 15%. The parameter they introduce, the Modified Crystal Deformation (MCD) is similar to the average grain orientation spread. It also shows a log-normal distribution. The results for the MCD are shown in Figure 5.1. The different system setups for the cases mentioned in the figure are listed in Table 5.1.

It can clearly be seen that for the MCD the same results are obtained as for the AGOS in this study, shown in Figure 4.29.

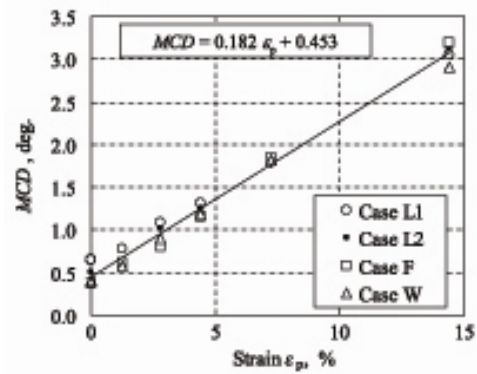


Fig 5.1 Modified crystal deformation measured against tensile strain by Kamaya et al. Different cases are listed in Table 5.1[5]

No.	System	Sample	Acc. voltage (kV)	Probe current (nA)	No. of points
Case L1	LEG	304SS	25	6	34,816–37,120
Case L2	LEG	304SS	15	20	23,296–25,344
Case F	FEG	304SS	25	Fixed	50,451
Case W	WEG	304SS	25	Fixed	12,288

Table 5.1 List of all different system setups for the scans on 304SS performed by Kamaya et al.[5]

The function for the MCD against the strain is given as:

$$MCD = 0.182\varepsilon_p + 0.453 \quad \text{Eq. 5.1}$$

while the function for the AGOS in the region below 20% of strain found in this study is:

$$AGOS = 0.168\varepsilon_p + 0.11 \quad \text{Eq. 5.2}$$

The difference in the functions found can be explained by the fact that the Kayama study uses a different material which of course has different properties. It can be concluded that both studies show similar results for the regime of 0% till 15% of strain. The study on JYH21CT shows that this linear behavior continues up to 22% and then goes to another linear regime from 20% up to 87% of strain, which can be written by the function:

$$AGOS = 0.068\varepsilon_p + 2.46 \quad \text{Eq. 5.3}$$

The misorientation gradient is strongly dependent on the step-size. A bigger step-size means a larger distance between two points, which results in a higher gradient for the same scanned area. This problem can be overcome by dividing the results by the distance between the points. The misorientation gradient will then be expressed in degrees per millimeter.

The results of the grain elongation in the models described in 4.7 – ‘Average grain shape aspect ratio’ show small deviations from experimental results for both: the surface and the bulk scans. The basic approximation used in these two models as well as in the OIM results analysis supposes that grains are elliptically elongated and all oriented with their long axis parallel to the tensile direction. As Figure 3.41 clearly demonstrates, the real shape and orientation of the grains are quite far from this expectation.

However, the model lines and experimental observations in Figure 3.41 show that the experimentally observed Average grain shape aspect ratio for the bulk grains follows the first model till a strain of 22%. Above 22% of strain the observations on the bulk grains seem to follow the second model. On the other side, the observed Average grain shape aspect ratio for surface grains follows the second model up to 40%. Above 40% of strain, the observations on the surface grain seem to tend to the first model.

The maximum strain at the surface of the sample bent with a radius of 1.5 mm is approximately 33%. On the tensile sample, almost no voids may be found below 36% of strain. This can explain why there has not been found any void on the bent sample. The hardness in the strained areas of the bent sample is significantly larger than in the undeformed area. The bending of the sample is performed with a three points bending test. With such a test, every point in the bent sample has a different moment. This causes a large gradient of strain throughout the whole sample. The grain orientation spread needs a lot of grains to get good statistics. Because there will be a large gradient of the strain in one scan, a three point bending test and OIM misorientation analysis is not a good combination. A four points bending test has a large region where the bending moment and surface tensile strain are constant. This results in larger areas with equal strains than with a three points bending test. For a good examination of a bent sample with OIM analysis, a four points bending test is recommended.

This study only deals with strain damage at room temperature inflicted under a constant strain rate. A recommendation for further study is to investigate strain damage on JYH21CT under conditions more close to the process route of its application (deep drawing).

6. Conclusions and Recommendations

- Both tested steels are in ferritic state (JPCD # 34-0396 – lattice parameter: 2.876 Å) after soft annealing. They show relatively strong texture characterized by these two preferential orientations:
 - $\langle 111 \rangle \parallel \text{ND}$
 - $\langle 001 \rangle \parallel \text{TD}$ & (001) inclined 45° to ND.

There is a substantial difference in grain size between AISI 410 and JYH21CT steel;

- Digital Image Correlation provides important information from material tensile straining: strain development in time or space may be observed as well as a reconstruction of true strain/stress curve is possible. Strain characteristics in necking region may be recorded as well to the very high strain values;
- Damage observation by OM and SEM together with fractography observations confirmed that hard TiN inclusions in JYH21CT steel are the main source of damage formed during plastic straining in a form of large voids;
- Damage characterization by void statistics does not give distinctive results. To obtain statistically more correct results, more data should be obtained by further investigation of voids. Two stages of damage accumulation by voids are observed. The first is a void initiation stage, the second is void growth;
- Both Aramis and OIM observations suggest that there are 2 stages of plastic deformation and damage accumulation: the first stage when strain $< 20\%$ and second stage when strain is larger than 20% ;
- Grain orientation spread, Grain misorientation gradient and Grain shape aspect ratio are the OIM parameters sensitive to accumulation of plastic deformation and damage. Grain orientation spread has a log-normal distribution inside plastically deformed grains;
- In the first stage characterized by slow strain rate, the fast accumulation of Grain orientation spread and Grain misorientation gradient is observed. In the second stage the Grain orientation spread grows slower in bulk grains and fully stops to grow in surface grains;
- A three points bending test does not lead to distinctive results in OIM observations. A four points bending test is recommended.

7. Acknowledgements

We would like to thank Philips Drachten in the person of dr. ir. Redmer van Tijum for providing the research topic and for the input during the investigation.

Great thanks goes out to our mentor dr. Vašek Ocelík who has taught us a lot about everything involving scientific research and writing a report.

We are thankful to prof. dr. Jeff de Hosson for the hospitality to let us do this research under the wings of the Material Science Department of the Rijksuniversiteit Groningen.

Ing. Gert ten Brink can not go unmentioned for his help in understanding the use of several techniques like OM, SEM and sample preparation.

We would like to say thanks to all MK group members for the hospitality and cooperation, directly or indirectly, with our research.

8. References

- [1] Aramis v.5.3.0 User Manual
- [2] Website: 'Oxford Instruments INCA crystal EBSD', <http://www.ebsd.com>
- [3] EDAX-TSL OIM Academy Course Manual Part 1 and 2
- [4] Website: 'Wikipedia, the free encyclopedia', <http://www.wikipedia.org>
- [5] Kamaya M. et al., 'Quantification of plastic strain of stainless steel and nickel alloy by electron backscatter diffraction', *Acta Materialia* 54 (2006) p. 539-548
- [6] Metals Handbook, Ninth Edition, Volume 12 – Fractography
- [7] Callister W.D., Materials science and engineering – An introduction, Sixth edition

Appendix

Grain Orientation Spread (GOS)

The grain orientation spread is a measure of the degree of misorientation within a grain. To calculate it, the central orientation of the grain is determined first by taking the average orientation of the grain.

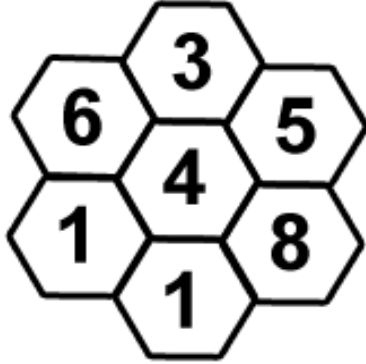


Fig A.1 Schematic picture of a grain containing 7 points with each point having a certain orientation indicated by a number

In the example of the grain in Figure A.1 the grain contains 7 points. Each point has an arbitrary orientation which is indicated by a number. The

central orientation is: $\frac{4 + 3 + 5 + 8 + 1 + 1 + 6}{7} = 4$

Now, the grain orientation spread is taken as the average of the difference of all points with respect to the central orientation:

$$\left\{ \begin{array}{l} |4 - 4| = 0 \\ |4 - 3| = 1 \\ |4 - 5| = 1 \\ |4 - 8| = 4 \\ |4 - 1| = 3 \\ |4 - 1| = 3 \\ |4 - 6| = 2 \end{array} \right\} \frac{0 + 1 + 1 + 4 + 3 + 3 + 2}{7} = 2$$

The grain orientation spread is hardly sensitive to the measurement system, system setup and step size (as concluded by Kamaya et al. [5]). Only when a very large step size is used, which will result in a few measuring points per grain, the grain orientation spread is inaccurate.

Misorientation Gradient

The misorientation gradient indicates the average change in orientation from point to point in a grain. It is calculated by first taking the difference in orientation for each pair of points within the grain and then taking the average of these differences. It is done below for the example grain of Figure A.1:

$$\frac{\left(\left\{ \begin{array}{l} |3 - 4| = 1 \\ |3 - 5| = 2 \end{array} \right\} + \left\{ \begin{array}{l} |5 - 4| = 1 \\ |5 - 8| = 3 \end{array} \right\} + \left\{ \begin{array}{l} |8 - 4| = 4 \\ |8 - 1| = 7 \end{array} \right\} + \left\{ \begin{array}{l} |1 - 4| = 3 \\ |1 - 1| = 0 \end{array} \right\} + \left\{ \begin{array}{l} |1 - 4| = 3 \\ |1 - 6| = 5 \end{array} \right\} + \left\{ \begin{array}{l} |6 - 4| = 2 \\ |6 - 3| = 3 \end{array} \right\} \right)}{12} = \frac{34}{12} = 2.83$$

The misorientation gradient is strongly dependent on the step size. A bigger step-size increases the distance between measured points, which can result in a whole different misorientation gradient.

Grain shape ellipses

For the calculation of the two parameters that will be explained next, the analysis program makes use of grain shape ellipses to approximate the shape of the grain. To draw an ellipse over the grain, the software uses the longest line it can draw within a grain as the major axis of the ellipse. It can then use three methods to calculate the minor axis of the ellipse. The first method uses the least squares method to minimize the squared error between the proposed ellipse and all of the grain boundary endpoints. The second uses the average width of the grain as the minor axis, while the third uses the constraint that the ellipse needs to cover the same area as the grain itself. In this research, the second method is used.

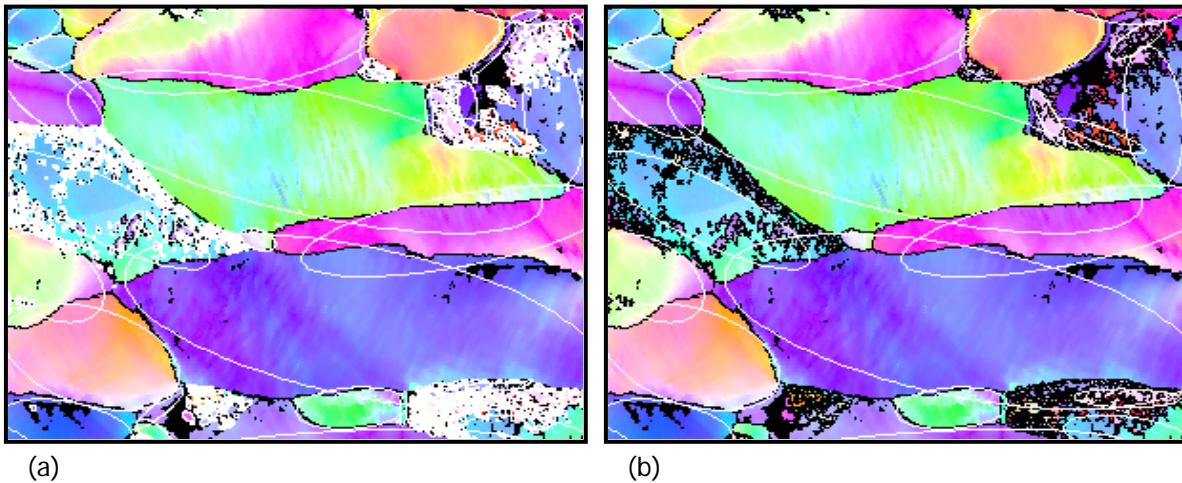


Fig A.2 Inverse Pole Figure Maps of scans of JYH21CT showing the grain shape ellipses taking a) all data and b) only grains containing more than 500 points

Figure A.2 shows two inverse pole figure maps of scans taken at 22% of strain on a JYH21CT sample. In Figure A.2a all data is taken into account. This results in very small shape ellipses over data points that lie within badly indexed areas. Because this will not give a representative result, a partition has been used which tells the software that only grains containing a minimum of 500 data points have to be taken into account. With this constraint, only the shape ellipses shown in Figure A.2b are used.

Grain shape aspect ratio

The grain shape aspect ratio is calculated by dividing the length of the minor axis of the ellipse by the length of the longer axis. For the calculation of the grain shape aspect ratio, it is important that grains are defined well, either by accurate scanning or good filtering of the data as explained in 'grain shape ellipses'.

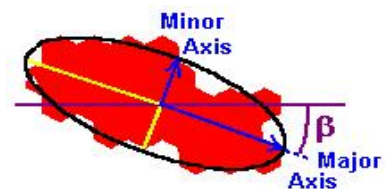


Fig A.3 One grain and its grain shape ellipse. The minor axis, major axis and the grain shape orientation β are indicated.

Grain shape orientation

The grain shape orientation gives a measure of the direction a grain is oriented in. It is defined as the angle between the major axis of the grain shape ellipse and the horizontal.

Pole figures and texture plots

Common ways to plot all directions present in a sample are the (inverse) pole figure and the texture plot. A pole figure shows the orientation of a certain direction of the crystal with respect to the sample coordinate system. An inverse pole figure shows the orientation of a certain direction of the sample with respect to the crystal coordinate system.

To get this 3D picture into a 2D plot, the method indicated in Figure A.4 is used. In the upper picture, the crystal is a cube inside a sphere with the sample coordinate system origin in its center. The crystal direction examined is indicated with orange lines. The crystal directions are projected on the sphere and indicated with orange dots. When looked at the sphere from the top (the normal direction in this case), the bottom picture of Figure A.4 can be seen. The orange dots are the same as in the upper picture, the white dots indicate the examined crystal direction in the bottom half of the sphere. By plotting the orange dots for all points in a scan, a pole figure is obtained. When a scan contains a large number of points, a texture plot tells you a lot more than just the pole figure. A texture plot indicates the density of dots with a color scale, while in a pole figure the large number of dots will make a big unidentifiable black blur. As an example, Figure A.5 shows an intensity plot, a contour plot and a pole figure, all belonging to the same scan.

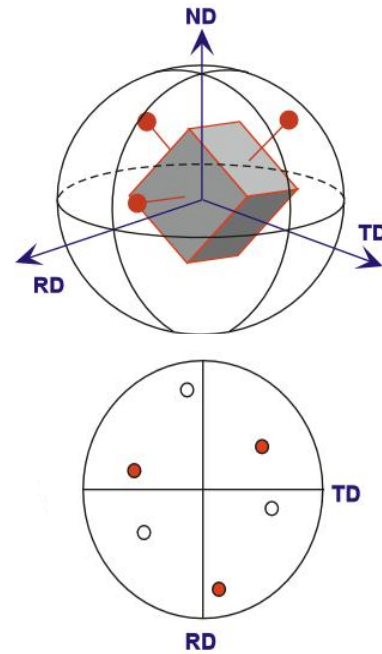


Fig A.4 The formation of a pole figure shown schematically.

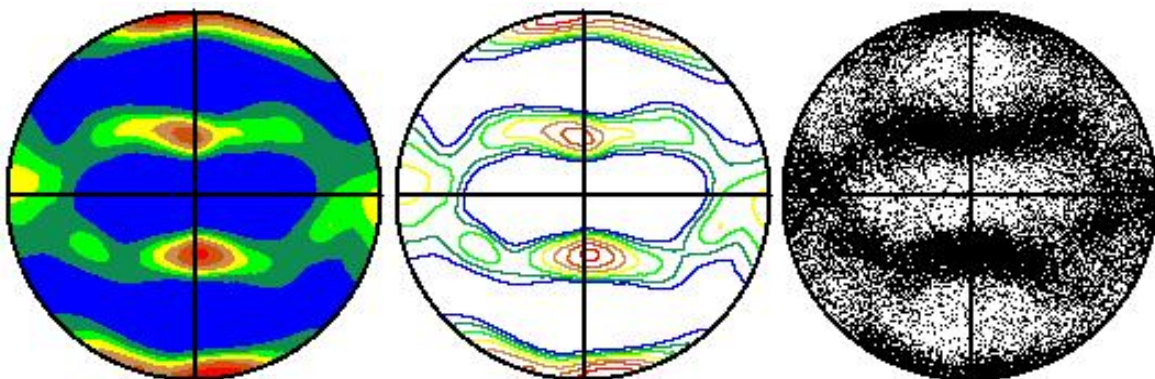


Fig A.5 Texture plots and pole figure of the same scan. From left to right: Intensity plot, contour plot and pole figure.